Energy Advances

ROYAL SOCIETY OF CHEMISTRY

REVIEW ARTICLE

View Article Online
View Journal | View Issue

Cite this: *Energy Adv.*, 2025, 4, 597

Recent advances in lanthanide-based metal–organic frameworks for photocatalytic hydrogen evolution applications

Peter Danita Patricia [a] and Rajadurai Vijay Solomon *[b]

Hydrogen is increasingly recognized as a promising clean fuel, offering a sustainable alternative to fossil fuels with water as its only combustion byproduct. Given several hydrogen production methods, photocatalytic water splitting stands out due to its potential for harnessing abundant solar energy to generate hydrogen. Among numerous photocatalysts reported for water-splitting, metal–organic frameworks (MOFs) exhibit excellent photocatalytic activity due to their enormous surface area. In this field, lanthanide-based MOFs (Ln-MOFs) have emerged as exceptional photocatalysts due to their unique properties and customizable structures, enhancing light absorption and charge separation. Recent advancements in the development of Ln-MOFs have demonstrated their potential to achieve notable hydrogen evolution rates under solar irradiation, positioning them at the forefront of renewable energy research. The introduction of Ln-MOFs into photocatalytic water-splitting marks a new era with a multitude of exciting possibilities ahead. In this context, a comprehensive overview of the trends and technologies involved in designing and understanding Ln-MOFs for water splitting is essential to developing efficient catalysts with enhanced properties. Here, we focus exclusively on the role of Ln-MOFs in photocatalytic water splitting, providing an in-depth analysis of their photocatalytic performance and stability. This review systematically classifies Ln-MOFs based on modifications in their frameworks, examining how these changes influence their properties and overall efficiency in hydrogen production. The review highlights the progress made in the field while addressing the gaps in current knowledge, particularly in understanding the mechanisms that govern the performance of Ln-MOFs. Moreover, it outlines future directions for enhancing the efficiency and stability of Ln-MOFs in hydrogen production, offering valuable insights that could guide further research. In summary, this review will aid the naïve and young researchers in the MOF domain to gain comprehensive knowledge on the nuances of lanthanide-based Ln-MOFs and appreciate their significant role in developing new technology for H_2 production.

Received 5th October 2024,
Accepted 4th March 2025

DOI: 10.1039/d4ya00560k

rsc.li/energy-advances

1. Introduction

The use of fossil fuels as conventional energy sources leads to greenhouse gas emissions, significantly impacting climate patterns.[1] With increasing concerns over climate change, hydrogen is recognized as a cleaner, sustainable alternative. Its clean combustion, high specific energy, storability, and generation of water as a byproduct make it an attractive replacement for traditional fuels.[2–6] Hydrogen is widely used in gas turbines,[7] aviation,[6] automotive fuel,[8,9] petroleum hydroprocessing,[10] and fuel cells.[11] To meet growing hydrogen demand sustainably, efficient production methods are critical. Hydrogen can be produced *via* steam methane reforming and methane pyrolysis from natural gas, producing CO_2 and carbon (soot), respectively (Fig. 1).[12,13] Coal gasification generates hydrogen with CO_2 as a by-product, contributing to the carbon footprint.[14] Alternatively, hydrogen is produced by anaerobic bacteria in artificial ecosystems under dark conditions, where complex sugars break down into organic acids and hydrogen, though the setup is costly and inefficient.[15] Thermal decomposition of ammonia or hydrocarbons can also generate hydrogen, with ammonia being CO_2-free but reliant on non-renewable sources, while hydrocarbons produce carbon by-products.[16,17] The most straightforward method of all is to produce hydrogen through water-splitting. This energy-driven process splits water molecules into oxygen and hydrogen with the help of a catalyst.[18–22]

[a] *MCC-MRF Innovation Park, Madras Christian College (Autonomous), East Tambaram, Chennai–600 059, Tamil Nadu, India*
[b] *Department of Chemistry, Madras Christian College (Autonomous), East Tambaram, Chennai–600 059, Tamil Nadu, India. E-mail: vjsolo@mcc.edu.in, vjsolo@gmail.com*

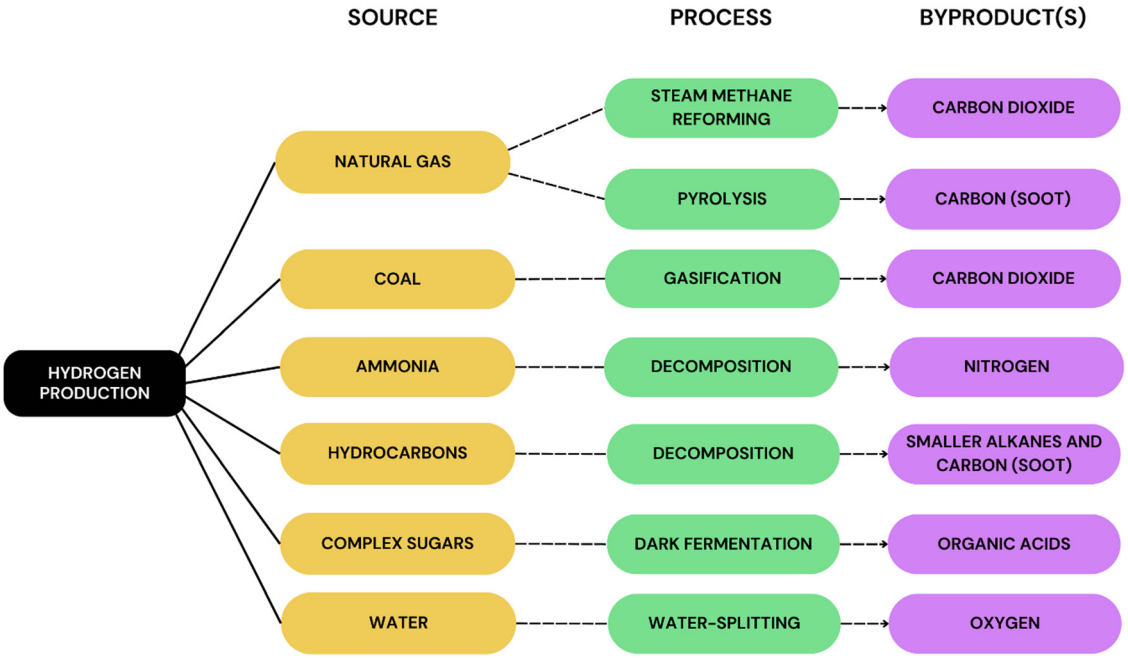

Fig. 1 Sources, processes and byproducts of several hydrogen production methods.

Water-splitting is an environmentally benign method for hydrogen production, offering zero carbon emissions and high efficiency (up to 80%).[23] Its only by-product is oxygen, which has no adverse environmental impact, and the water source is abundant. This sustainable process can be driven by thermal, biochemical, photonic, or electrical energy (Fig. 2).[20,24] Thermal water splitting occurs at temperatures above 2500 K, but it faces challenges such as complex reaction kinetics and the need for cooling material recovery.[19] Biochemical water splitting, involving cyanobacteria and algae in direct photolysis, is greener but hindered by low efficiency, high costs, and large operational areas.[18]

Electrolysis is another widely known method, where water is split into hydrogen and oxygen by electricity. Hydrogen evolves at the cathode *via* the hydrogen evolution reaction (HER) and oxygen at the anode *via* the oxygen evolution reaction (OER).[25,26] However, this method requires high energy input and struggles with scalability.[24] To overcome these limitations, photocatalytic water-splitting has emerged as an alternative. This process uses solar energy (photons) and a catalyst to

P. Danita Patricia

Danita Patricia received her Bachelors degree in Chemistry at Madras Christian College, Tambaram, India. She obtained her MSc in Chemistry in 2024 from Loyola College, Chennai, India. She carried out this work during her internship at MCC-MRF Innovation Park, Madras Christian College, Chennai, India, under the guidance of Dr R. Vijay Solomon. Her research specializes on metal–organic frameworks (MOFs) for environmental applications, and high temperature solid-state synthesis in inert atmosphere.

Rajadurai Vijay Solomon

Dr Rajadurai Vijay Solomon, hailing from Tirunelveli, Tamil Nadu, earned his Bachelor's degree from St. Xavier's College, Master's degree from Bishop Heber College, and PhD from Bharathidasan University under Prof. P. Venuvanalingam, focusing on designing molecules for materials and biomaterials. Awarded the prestigious Swiss Excellence Fellowship in 2012, he worked with Prof. Markus Meuwly at the University of Basel and later joined Prof. Andreas Heyden's catalysis group at the University of South Carolina (2014–2016) as a postdoctoral associate. Since 2016, he has been serving as an Assistant Professor of Chemistry at Madras Christian College, publishing over 110 research articles and securing funded projects.

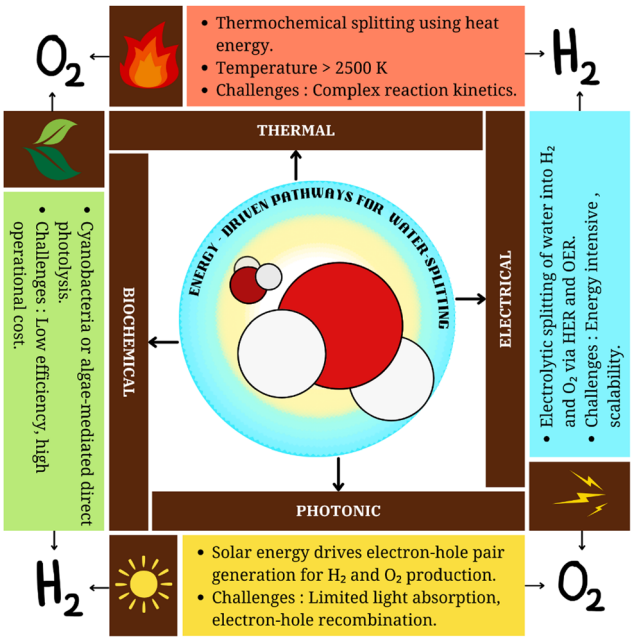

Fig. 2 Various energy-driven pathways through which water can be split into its constituents.

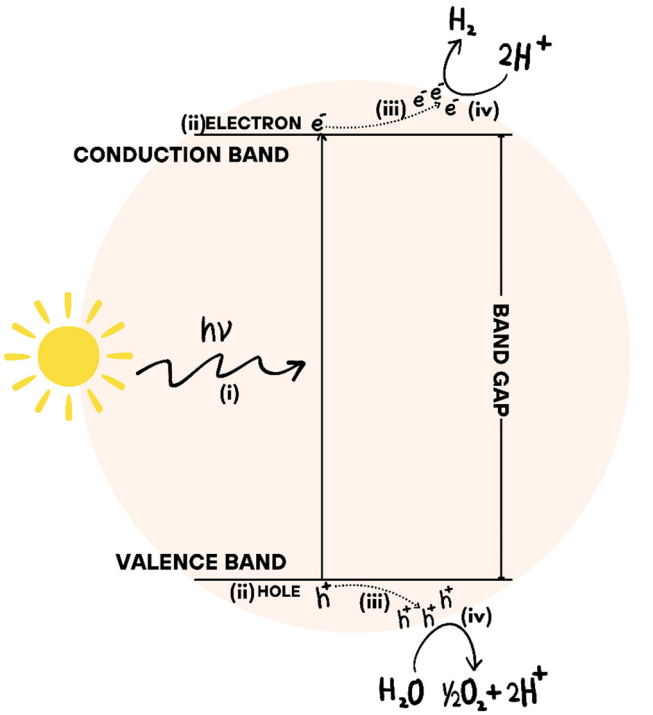

Fig. 3 Key steps involved in the photocatalytic water-splitting process: (i) photon absorption; (ii) electron–hole generation; (iii) carrier separation and migration; and (iv) redox reactions at the surface.

generate electrons and holes that split water into hydrogen and oxygen. Photocatalytic water-splitting, or photocatalytic hydrogen evolution (PHE), is highly efficient, as a significant portion of solar photons can be utilized in the presence of an effective catalyst.[24] This approach minimizes energy conversion losses and represents a promising path toward sustainable hydrogen production.

2. Fundamentals of PHE

PHE involves four steps: (i) photon absorption, (ii) electron–hole pair generation, (iii) carrier separation and migration, and (iv) surface reactions producing H_2 and O_2 (Fig. 3). The process relies on photocatalysts, photosensitizers (PSs), and sacrificial donors (SDs).

Upon light irradiation, electrons (e^-) in the photocatalyst's valence band (VB) are excited to the conduction band (CB), leaving holes (h^+) behind (I). Holes oxidize water, generating protons (II), which are reduced by CB electrons (III), forming H_2 and O_2. The overall reaction is summarized below (IV).[27–29]

$$\text{On irradiation,} \quad 2h\nu \rightarrow 2e^- + 2h^+ \qquad \text{(I)}$$

$$\text{Oxidation,} \quad 2h^+ + H_2O_{(l)} \rightarrow 1/2O_{2(g)} + 2H^+ \qquad \text{(II)}$$

$$\text{Reduction,} \quad 2H^+ + 2e^- \rightarrow H_{2(g)} \qquad \text{(III)}$$

$$\text{Overall reaction,} \quad 2h\nu + H_2O_{(l)} \rightarrow 1/2O_{2(g)} + H_{2(g)} \qquad \text{(IV)}$$

Photocatalysts enhance reaction rates by improving photogenerated carrier separation and enabling broad-spectrum light absorption, providing more photons for the reaction. When light energy exceeds the band gap, electron–hole pairs form. For water splitting, the CB must be more negative than the H^+ reduction potential and the VB more positive than the water oxidation potential.[29] Although water splitting requires 1.23 eV, practical applications require a band gap of 1.6–2.2 eV.[30] Smaller band gaps enable wider light absorption, while crystallinity, particle size, and structure affect charge separation. Higher crystallinity reduces defects, improving charge mobility and minimizing recombination, whereas nanometer-sized particles enhance charge transfer but may increase recombination if too small. Cocatalysts are essential for enhancing the performance of semiconductor photocatalysts in H_2 evolution. Plasmonic metals like Au and Cu improve visible light absorption through localized surface plasmon resonance (LSPR) effects.[31,32] By attracting electrons, cocatalysts facilitate efficient separation of electron–hole pairs and enhance charge carrier transfer when integrated with photocatalyst surfaces.[33,34] Additionally, they provide active sites for photocatalytic reactions, functioning as electron sinks and proton reduction sites.[35,36] Cocatalysts also improve the stability of photocatalysts, particularly metal sulfides, by extracting photogenerated holes, thereby preventing self-decomposition and supporting oxygen evolution reactions, ultimately boosting overall photocatalytic efficiency.[37,38]

PSs harvest sunlight and initiate redox reactions for solar fuel generation by absorbing photons and exciting an electron to form PS*. PS* undergoes reductive or oxidative quenching and is regenerated in catalytic reactions, producing solar fuels like hydrogen or reducing CO_2. Efficient PSs require long excited state lifetimes for electron transfer and should absorb a broad light spectrum, especially visible light, to optimize sunlight utilization.[39–43] SDs are essential in artificial

photosynthesis, particularly for water splitting. Acting as electron sources, they sustain electron flow, prevent reverse reactions with oxidized products like oxygen, and ensure continuous hydrogen production. Effective systems require compatible redox potentials between PSs and SDs, accounting for the excited state lifetime and catalytic needs of PSs. SDs are irreversibly oxidized, enabling PS operation but generating chemical waste and requiring replenishment, which reduces sustainability.[44–47] PSs also face photobleaching and back electron transfer, causing side reactions and lower efficiency.[43] Research aims to develop photocatalysts that drive water splitting independently, eliminating reliance on SDs and PSs, thus improving efficiency and sustainability.

In recent decades, numerous photocatalysts have been explored for water splitting. TiO_2, studied since the 1970s, remains a key material due to its abundance, stability, and favorable band alignments. However, its wide band gap (3.2 eV) limits light absorption to the UV region, and issues with conductivity and recombination persist.[48] Improvements include band gap modification, nanostructuring, defect control, co-catalyst decoration, and heterojunctions. Other materials like Fe_2O_3, WO_3, ZnO, $BiVO_4$, Cu_2O, and CdS offer narrower band gaps (2.0–2.5 eV) but face challenges such as low carrier mobility and crystallographic disorder.[49–58] Emerging materials, including graphene-based materials, perovskites (*e.g.*, $CH_3NH_3PbI_3$, $CsPbBr_3$), and 2D materials (*e.g.*, MoS_2, g-C_3N_4), show promise due to their unique properties. However, they face issues with light absorption, stability, scalability, toxicity, and synthesis.[59–63] In addition, covalent organic frameworks (COFs), conjugated porous polymers (CPPs), and porphyrins are promising photocatalysts for water splitting due to their distinct features. COFs offer tunable band gaps,

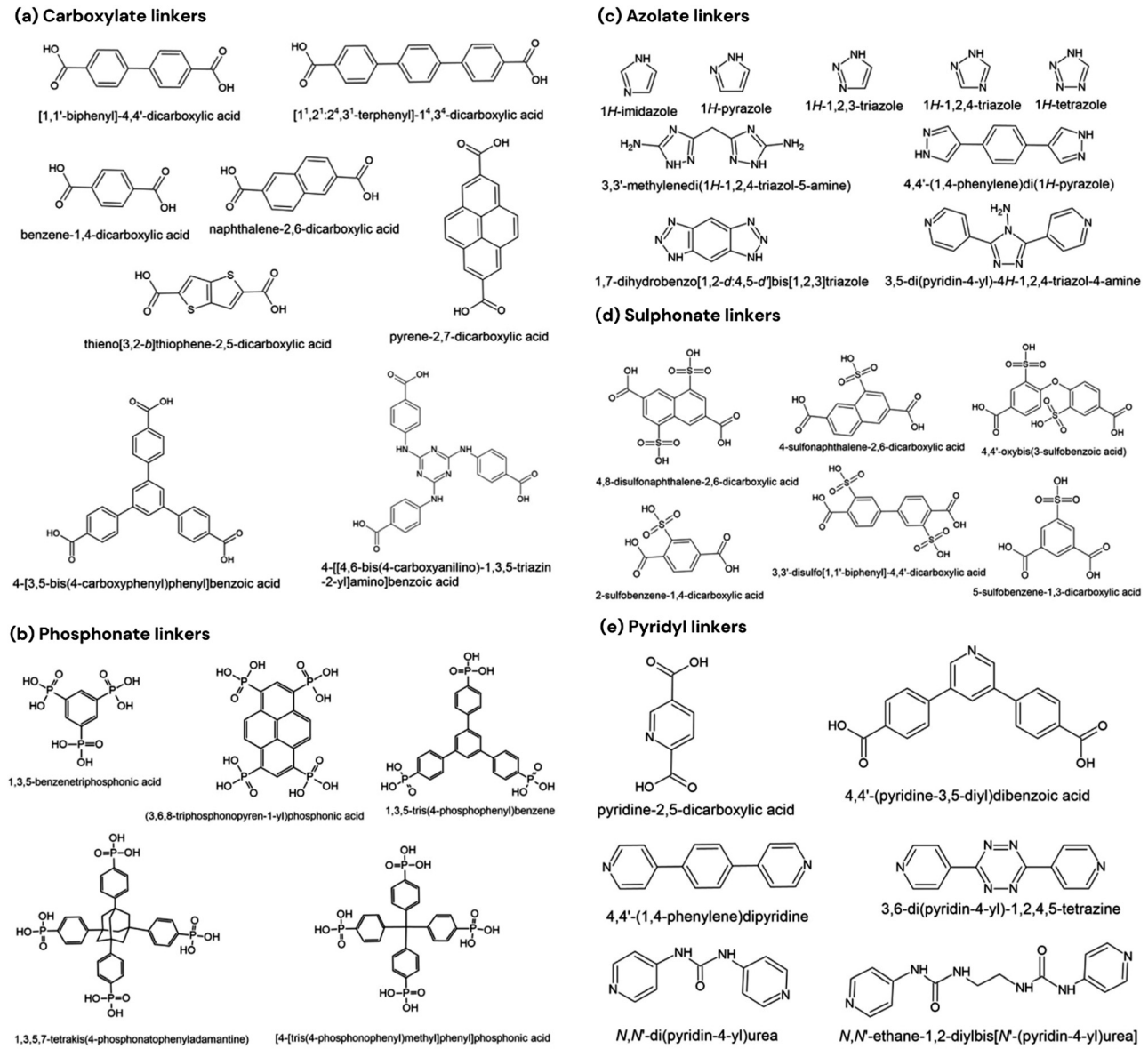

Fig. 4 Some representative examples of ligands: (a) carboxylate, (b) phosphonate, (c) azolate, (d) sulphonate and (e) pyridyl.

high porosity, and extended π-conjugation for efficient charge separation and light absorption.[64,65] CPPs exhibit broad visible-light absorption and delocalized π-electrons, enhancing charge transport.[66,67] Porphyrins serve as efficient light-harvesters and electron transfer agents, functioning as both photosensitizers and catalytic sites.[68–70] However, metal–organic frameworks (MOFs) surpass these materials with abundant catalytic sites, exceptional structural tunability, and superior photocatalytic performance due to the presence of metal centers, positioning them as frontrunners in water-splitting applications.

MOFs are crystalline structures formed by coordinating organic linkers with metal ions or clusters that offer high porosity and versatility. Constructed from metals like transition metals, lanthanides, and actinides, mixed-metallic MOFs incorporate multiple metals.[71] Organic linkers, including carboxylate, azolate, phosphonate, sulfonate, and pyridyl groups, enable diverse structures from 1D chains to 3D networks.[72,73] Some representative examples of linkers from each class are depicted in Fig. 4. The general classification of MOFs based on porosity, dimensionality, type of node, type of linker, and topology is presented in Table 1. Certain MOFs have rigid frameworks, ideal for harsh environments, while flexible ones enable reversible gas adsorption.[74] High-valent metals and rigid linkers enhance thermal stability, making MOFs adaptable for addressing limitations in conventional materials.

MOFs are renowned for high porosity, vast internal surface areas, and tunable pore sizes, making them ideal for gas storage, separation, and catalysis.[113,114] By varying linker lengths, MOFs achieve selective gas capture, such as CO_2 from flue gas, and hydrocarbon separation in petrochemical processes.[72,115,116] Their modular synthesis enables functional group introduction during or after synthesis, enhancing trapping and catalytic performance.[117–119] Many MOFs are biocompatible for drug delivery, while others excel in heterogeneous catalysis due to large surface areas, tunable pore sizes, and catalytic active sites.[72,120–123] Catalytic MOFs integrate metal ions, clusters or functionalized linkers, with porosity allowing easy access to active sites.[124] MOFs maintain structural integrity after post-synthetic modifications, enhancing versatility.[28]

Table 1 General classification of MOFs based on dimensionality, porosity, type of organic linkers, topology and type of metal nodes

Classification	Types	Examples	Ref.
Dimensionality	1-Dimensional	IMP-27Na	75
		MIL-132	76
		Mg-MOF-74	77
		CAU-50	78
	2-Dimensional	ULMOF-1	79
		AgPb-MOF	80
		CTH-15	81
		COK-47	82
	3-Dimensional	MOF-808	83
		KGF-1	84
		CAUMOF-8	85
		CdNa-MOF-1	86
Porosity	Microporous (<2 nm)	ZIF-8	87
		MOF-508	88
		$[Zn(bdc)(ted)_{0.5}]\cdot 2DMF\cdot 0.2\ H_2O$	89
		$[Cu(INA)_2]$	90
	Mesoporous (2–50 nm)	MIL-100(Cr)	91
		ZIF-100	92
		MOF-180	93
		NOTT-116(PCN-68)	94
Type of organic linker	Carboxylate	FeNi-DOBDC	95
		CoNi-MOFNA	96
	Azolate	ZIF-8	97
		ZIF-67	98
	Pyridyl	$\{[Cu^{I}I][Cu^{II}(pdc)(H_2O)]\cdot 1.5MeCN\cdot H_2O\}_n$	99
		67BPym-MeI	100
	Sulphonate	PAMPS@MIL-101-SO_3H	101
		UiO-66-SO_3H	102
	Phosphonate	IPCE-1Ni	103
		TUB75	104
Type of metal nodes	Single Clusters	MIL-53(Fe)	105
		UiO-66	106
		NH_2-MIL-125	107
Topology	Simple	MOF-5	108
		HKUST-1	109
		ZTF-1	110
	Complex	PCN-222	111
		MOF-74	112

As photocatalysts, MOFs absorb light and generate reactive species for pollutant degradation and water-splitting. Their ability to absorb broad-spectrum light supports electron–hole generation and efficient charge separation.[125] The first MOF photocatalyst Al-ATA consists of $AlO_4(OH)_2$ octahedral clusters linked by 2-aminoterephthalate (ATA). Incorporating Ni(II) enabled Al-ATA to produce hydrogen at 36.0 μmol h^{-1}, establishing it as the first water-splitting photocatalyst.[126] Another breakthrough was MIL-125-CoPi–Pt, with cobalt phosphate (CoPi) and Pt cocatalysts, which reached H_2 and O_2 production rates of 42.33 μmol h^{-1} and 21.33 μmol h^{-1}, suppressing electron–hole recombination.[127] In another instance, MIL-125-NH_2 with Pt and RuO_x cocatalysts enhanced H_2 and O_2 production to 85 μmol g^{-1} and 218 μmol g^{-1} over 24 h, achieving 0.32% quantum efficiency.[128] Introducing defects, such as plasma-treated Ti-oxo clusters in MIL-125-NH_2, improved the photocatalytic activity.[129]

Despite advancements, transition metal MOFs often show low light response, necessitating cocatalysts. Incorporating lanthanides into MOFs has emerged as a solution. Lanthanide-based MOFs (Ln-MOFs) exhibit high coordination numbers, well-defined energy levels, luminescence, and catalytic properties.[130–132] Combining lanthanide properties with MOFs opens opportunities for tailored photocatalytic water splitting.[133,134] This review explores Ln-MOFs in photocatalytic water splitting, discussing their structural diversity, optical properties, and catalytic efficiencies.

3. Scope of the review

Since 2017, when An *et al.* first introduced the concept of MOFs as photocatalysts for hydrogen production *via* water-splitting, the field has seen a surge in research activity.[126] Numerous studies have since explored the potential of MOFs and their derivatives in this domain, highlighting their unique structural advantages and catalytic capabilities. The ongoing interest in MOF-based photocatalysis has led to the publication of several comprehensive reviews, each summarizing the latest advancements and providing insights into various aspects of this technology (Table 2).[135–148] Reddy *et al.* provide a comprehensive analysis of MOF-based heterogeneous photocatalysts, highlighting applications in hydrogen generation, CO_2 reduction, and organic dye photodegradation.[135] On the other hand, Liu *et al.* have focused on the photocatalytic hydrogen production applications of MOF-based materials across the UV, visible, and near-IR regions.[136] Luo *et al.* classify MOF-based and MOF-derived photocatalysts, elucidating how modifications enhance photocatalytic performance.[137] Nguyen's review identifies key achievements and limitations in MOF photocatalysts for water splitting, suggesting future research directions.[138] Xiao *et al.* emphasize MOF-based heterostructures for hydrogen production, particularly the factors affecting interfacial charge transfer.[139] Nordin *et al.* review synthetic methods, surface functionalization, elemental doping, ligand modification, and heterojunction techniques to improve MOF photocatalytic properties.[142] Sun *et al.* discuss advances in photocatalytic water splitting and CO_2 reduction using MOF-based materials, emphasizing structural features influencing catalytic activity.[141] Despite extensive research on MOFs, the photocatalytic water-splitting applications of lanthanide-based MOFs (Ln-MOFs) remain underexplored. Most reviews focus on broader catalytic applications of rare earth (RE) MOFs. For instance, Sun *et al.* summarize RE-MOFs for organic reactions,

Table 2 Pros and cons of the previously existing reviews and the strengths of the current review

Review	Pros	Cons	Strengths of this review
Reddy *et al.*[135]	Comprehensive analysis of MOF-based heterogeneous photocatalysts for various applications, including H_2 generation	Limited focus on Ln-MOFs and photocatalytic water splitting	Dedicated focus on Ln-MOFs for hydrogen production, filling the gap in prior studies
Liu *et al.*[136]	Explores photocatalytic hydrogen production across UV, visible, and near-IR regions	Does not specifically highlight Ln-MOFs or modifications enhancing PHE performance	Provides a detailed exploration of the unique properties of Ln-MOFs for enhanced photocatalysis
Luo *et al.*[137]	Framework for understanding how MOF modifications enhance photocatalytic performance	General MOF focus with limited mention of Ln-MOF-specific applications	Offers specific insights into Ln-MOF modifications and their effects on water splitting
Nguyen *et al.*[138]	Identifies key achievements and limitations in MOF photocatalysts for water splitting	Does not detail the unique role of lanthanides in MOF-based water-splitting photocatalysis	Highlights the distinctive advantages of lanthanide metals in water-splitting applications
Xiao *et al.*[139]	Emphasis on heterostructures and interfacial charge transfer for enhanced photocatalysis	Neglects lanthanide-specific systems and applications in photocatalytic water splitting	Provides an in-depth analysis of Ln-MOF-based heterostructures for PHE performance
Nordin *et al.*[139]	Extensive overview of synthetic methods and functionalization techniques for MOFs	Limited discussion on lanthanides and their specific photocatalytic capabilities	Explores Ln-MOF-specific synthesis and functionalization for optimal PHE performance
Sun *et al.*[141]	Highlights advances in water splitting and CO_2 reduction using MOF-based materials	Minimal focus on lanthanide-based systems and their unique contributions	Offers a comprehensive review of Ln-MOFs specifically for hydrogen production
Zhang *et al.*[148]	Detailed synthesis methods and applications of RE-MOFs in various fields	Lacks a focused discussion on Ln-MOFs as catalysts in PHE	Exclusively examines Ln-MOFs for PHE
Shi *et al.*,[144] Fan *et al.*,[145] Meng *et al.*[146]	Highlights general RE-MOF applications in energy and environmental catalysis	Limited insights into lanthanide-specific photocatalytic water-splitting capabilities	Bridges the gap by providing detailed analysis of Ln-MOFs in water-splitting technologies

photocatalysis, and CO oxidation but do not address Ln-MOFs in water splitting.[140] Saraci *et al.* classify RE-MOFs by metal composition, discussing sensing, imaging, and catalysis without emphasis on water splitting.[143] Similarly, Shi *et al.* review RE-MOFs in energy conversion but provide limited insights into their photocatalytic water-splitting potential.[144]

Fan *et al.* explore RE-modified MOFs for photo/electrocatalysis, emphasizing the theoretical advantages of RE elements in MOF modification but lacking specific discussion on Ln-MOFs for water splitting.[145] Meng *et al.* address photocatalytic and electrocatalytic applications of RE-MOFs, including hydrogen evolution and CO_2 reduction, but again do not focus on Ln-MOFs in water splitting.[146] Zhang *et al.* review RE-MOF synthesis and photon-related applications, including fluorescence detection and luminescence, emphasizing Ce, Eu, Tb, Yb, and Gd but only briefly addressing water splitting.[147] Zhang *et al.* also summarize the catalytic applications of Ln-MOFs, including photocatalysis, but further exploration of their role in water splitting is warranted.[148] This review is one of the few that specifically addresses the role of lanthanides in MOF-based catalysis, but it still leaves room for a more detailed exploration of their use in water splitting. Here is a table summarizing the pros and cons of the previously existing reviews, along with the strengths of the current manuscript.

Given the limited focus on lanthanide-based MOFs in the existing literature, there is a clear need for a dedicated review that comprehensively examines their applications in photocatalytic water splitting. Such a review would not only fill a significant gap in the current body of knowledge but also provide valuable guidance for future research in this promising area. Therefore, this review aims to exclusively discuss the application of various Ln-MOFs and their derivatives for hydrogen production through the PHE process, offering a detailed analysis of the latest advancements in the past 10 years and highlighting potential areas for further exploration. Relevant articles were gathered using the Google Scholar search engine. Additionally, special issues focusing on the catalytic applications of MOF materials were instrumental in identifying related studies.[149–151]

4. Lanthanide MOFs for PHE

When the catalytic properties of MOFs began to be understood in the early 2000s, Ln-MOFs started to gain significant attention around the mid-2010s. These frameworks were initially explored for their unique luminescent properties. In 2007, researchers such as Chen *et al.* and Cheng *et al.* delved into the luminescent characteristics of lanthanide metal nodes within MOFs, investigating their potential applications in sensing technologies.[152,153] The journey into understanding MOFs deepened in 2012 when Ramya *et al.* conducted studies on energy transfer within these metal nodes.[154] They focused on the energy transfer from a terbium (Tb^{3+}) center to a europium (Eu^{3+}) center in a mixed-lanthanide MOF. This work set the stage for further exploration into the photophysical properties of these materials. Subsequently, Lin and Zhang provided a comprehensive overview of energy transfer processes and light-harvesting capabilities in Ln-MOFs, highlighting their potential in various photonic applications.[155] In 2019, a notable breakthrough occurred with the report of a La-MOF for hydrogen generation. The material was found to have a band gap of 3.1 eV. Through cyclic voltammetry, the LUMO energy was determined to be −2.5 V, which is more negative than the reduction potential of hydrogen, suggesting that the MOF could be effectively used to generate hydrogen, opening new avenues for clean energy applications.[156] Following this, in 2020, researchers studied the effects of incorporating lanthanides into the nodes of UiO-66, a well-known MOF, on its catalytic activity.[157] This research provided valuable insights into the catalytic behavior of Ln-MOFs, demonstrating their potential in various catalytic processes.

These light-harvesting properties of Ln-MOFs originate from the lanthanide metals present in the MOFs. These lanthanides display special optical properties owing to the 4d electron layer in the metals, thereby activating the framework under photo-excitation conditions. Additionally, the 4f orbitals, shielded by the filled 5s and 5p subshells, create multiple low-lying empty states in the 4f shell.[130] These orbitals are responsible for the unique electronic properties of lanthanides, leading to sharp emission lines and long-lived excited states. These characteristics make lanthanides suitable candidates to strengthen the light-harvesting nature of MOFs. Incorporation of lanthanides into MOFs can effectively modify the bandgap and electronic structure of the material. Furthermore, Ln-MOFs exhibit high photostability, ensuring structural integrity and catalytic activity for prolonged periods of irradiation.[158] Ln-MOFs hold great promise in the realm of PHE due to their permanent porosity, impressive structural diversity, high coordination number, and the flexible coordination environment of lanthanides.[133,159] One of the key features of these MOFs is their ability to incorporate functional organic ligands, support and convert into various derivatives.[160,161] The desirable qualities of Ln-MOFs, such as high surface area, tunable pore size, and chemical and thermal stability, make them excellent candidates for catalysts.[148] By leveraging the properties of lanthanides, Ln-MOFs can achieve efficient charge separation and transfer, reduced recombination rates, and thereby increased overall efficiency in photocatalytic water-splitting applications.

This review aims to highlight the performance and stability of various Ln-MOFs in PHE applications, drawing from case studies to illustrate their potential. The graphical overview provided in Fig. 5 encapsulates the topics of discussion that follow.

4.1. Differing node composition

To enhance the photo-response of MOFs, one effective strategy is to incorporate a different transition metal into the framework, aside from the one already constituting the secondary building units (SBUs). This subsection discusses the effect of the incorporation of various lanthanide metals into a single MOF framework with the help of a few relevant studies. This mixed-metal approach facilitates electron transfer from one

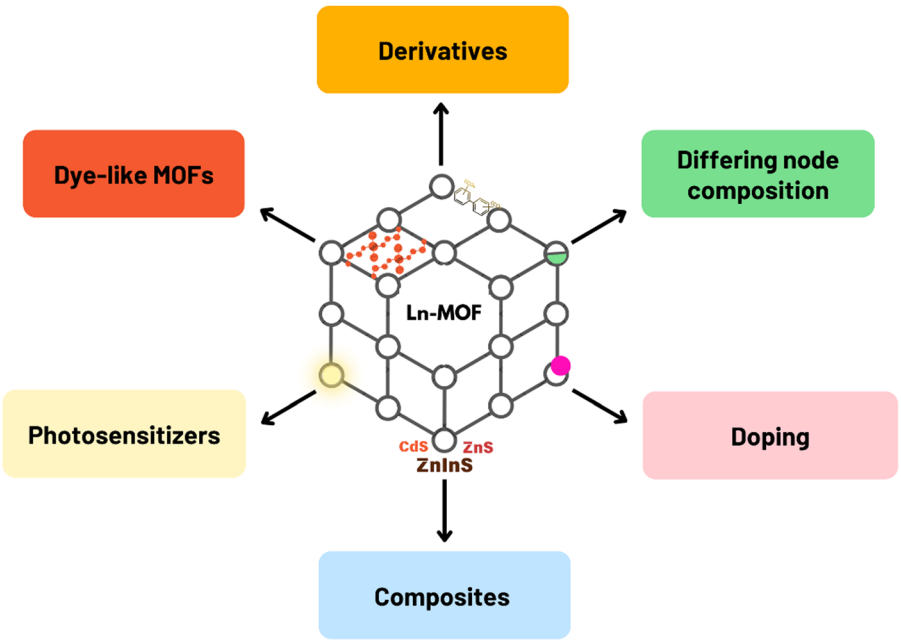

Fig. 5 A graphical overview illustrating various Ln-MOF modifications.

metal to another, thereby decreasing the band gap and increasing charge separation efficiency. In this context, incorporation of Ce^{4+} into the framework is said to increase the efficiency of the catalyst, due to the low-lying empty 4f orbitals of the lanthanide.[162,163]

In 2020, a study by A. Melillo *et al.* examined the catalytic activities of a series of five UiO-66(M: Zr, Zr/Ti, Zr/Ce, Zr/Ce/Ti, Ce) materials for overall water-splitting. It was found that the activity of the trimetallic MOF was seven times higher than that of its single metal analogue that contained only Zr.[157] The band gap of the trimetallic MOF was determined to be 3.10 eV with the help of UV-DRS. This makes UiO-66(Zr/Ce/Ti) a suitable catalyst for water splitting, since at pH 7 the CB energy must be higher than −4.03 eV for the evolution of H_2 from water. Among the five members, the catalytic activity for overall water splitting followed the order UiO-66(Zr/Ce/Ti) > UiO-66(Zr/Ti) > UiO-66(Zr/Ce), whose activities were higher than that of the single metal MOF, when irradiated with a xenon laser in the presence of a cut-off filter ($\lambda > 450$ nm).[157] The quantum yields for the reactions were found to be 0.55, 0.055, and 0.1 at 300 nm, 400 nm and 500 nm, respectively, indicating the highest relative efficiency at 300 nm. However, the maximum amount of hydrogen was generated at 400 nm (Fig. 6a). Reusing the UiO-66(Zr/Ce/Ti) catalyst caused a minor decrease in the initial rate of reaction as well as the final volume of hydrogen produced (Fig. 6b). The use of a sacrificial donor, namely methanol, along with the MOF, resulted in the increase of the amount of hydrogen production by two-fold, up to 390 μmol g^{-1} in 22 hours. This is much higher than that of individual UiO-66 (∼155 μmol g^{-1}).[157]

Cerium plays a multifaceted role in UiO-66(Zr/Ce/Ti), enhancing photocatalytic activity through improved charge separation, increased light absorption, enhanced structural stability, and synergistic interactions with other metals. The improved photocatalytic efficiency of the MOF was attributed to kinetic factors like charge separation and recombination rather than thermodynamic factors like band gap alignment.[157]

Following this, in 2023, two MOFs, Eu-MOF-Ru(cptpy)$_2$ and Pr-MOF-Ru(cptpy)$_2$, were synthesized using the ruthenium complex Ru(cptpy)$_2$ as the organic linker, with europium (Eu(III)) and praseodymium (Pr(III)) ions serving as the metal nodes, respectively. To enhance their catalytic performance, platinum (Pt) nanoparticles were photodeposited onto the surfaces of the MOFs, acting as co-catalysts. The catalytic performance was evaluated in a triethanolamine aqueous solution, which served as a sacrificial agent. For Pr-MOF-Ru(cptpy)$_2$, an optimal H_2 evolution rate of 268 μmol g^{-1} h^{-1} was achieved with a 1.5% Pt loading. However, when ascorbic acid (AA) was used as a sacrificial reagent, the H_2 evolution rate significantly increased to 1047 μmol g^{-1} h^{-1} (Fig. 6c). This enhancement was attributed to the better matching of the redox potential of AA with the VB of the Pr-MOF, facilitating more efficient electron transfer. In contrast, Eu-MOF-Ru(cptpy)$_2$ exhibited superior photocatalytic performance with a lower Pt loading of 0.5%, achieving an impressive H_2 evolution rate of 4373 μmol h^{-1} g^{-1} in the presence of ascorbic acid. The apparent quantum efficiency (AQE) of this catalyst was measured at 0.79% at 500 nm, indicating its excellent ability to absorb and utilize visible light for photocatalysis (Fig. 6d).[164]

The Eu-MOF catalyst also demonstrated remarkable stability; it maintained its catalytic activity over 9 hours of continuous reaction, showing little to no degradation (Fig. 7a). In contrast, the Pr-MOF catalyst exhibited a significant decrease in activity over the same period, likely due to instability in the

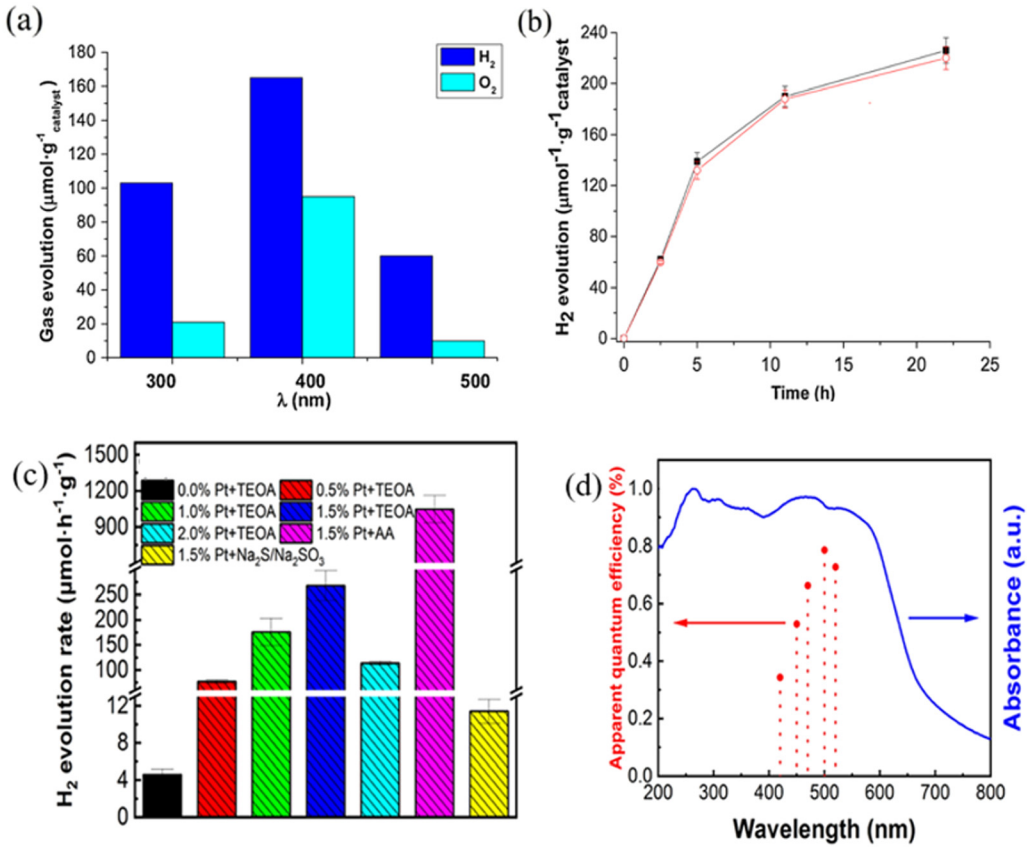

Fig. 6 (a) Diffuse reflectance UV-Vis spectra of (a) UiO-66(Zr), (b) UiO-66(Zr/Ti), (c) UiO-66(Zr/Ce), (d) UiO-66(Zr/Ce/Ti), and (e) UiO-66(Ce). The inset (on the right) corresponds to a magnification of the 400–650 nm region for (a)–(d). (b) Photocatalytic H_2 evolution in the overall water splitting for two consecutive uses of UiO-66(Zr/Ce/Ti): first use (■) and second use (○). Reprinted with permission from ref. 157. Copyright 2020 Elsevier. (c) H_2 evolution rates of Pr-MOF-Ru(cptpy)$_2$ catalysts under different conditions. (d) Wavelength dependence of the AQE of 0.5% Pt/Eu-MOF-Ru(cptpy)$_2$. Reprinted with permission from ref. 164. Copyright 2023 ACS.

ascorbic acid solution, which led to the decomposition of the MOF structure (Fig. 7c). These findings highlight the potential of Eu-MOF-Ru(cptpy)$_2$ as a highly efficient and stable photocatalyst for hydrogen production under visible light, with a lower requirement for Pt loading and better performance compared to Pr-MOF-Ru(cptpy)$_2$.[164]

Another recent study by Gu *et al.* focuses on the PHE activity and stability of a cerium-based MOF called CSUST-4, along with its lanthanide-substituted variants (CSUST-4-Ln, where Ln = La, Nd, Eu, Er, Yb). CSUST-4 was synthesized using a solvothermal method, yielding a 3D porous framework with significant potential for photocatalysis due to its bandgap of 3.04 eV and n-type semiconductor properties. The catalytic activity was assessed under simulated sunlight in the presence of triethylamine (TEOA) as a sacrificial agent and Pt as a co-catalyst. Activated CSUST-4 showed an improved hydrogen evolution of 41 μmol g^{-1} over 6 hours, compared to 34 μmol g^{-1} for the as-synthesized version (Fig. 7e).[165]

This improvement is attributed to the exposure of open Ce(III) sites, which enhanced interactions with water molecules, thereby boosting catalytic efficiency. When examining the stability and performance of lanthanide-substituted variants, CSUST-4-Nd demonstrated the highest hydrogen evolution (71 μmol g^{-1} in 6 hours), followed by CSUST-4-Er (61 μmol g^{-1}). These MOFs outperformed the base CSUST-4, while CSUST-4-Eu, CSUST-4-La, and CSUST-4-Yb exhibited lower activities, likely due to their limited visible light absorption and differing electronic properties. The band gap values of all the CSUST MOFs studied are provided in Fig. 7f. The study highlights that the catalytic activity and stability of these MOFs are closely linked to the specific lanthanide ion used, with Nd and Er proving most effective for enhancing hydrogen production through water splitting.[165]

4.2. Doping metals

MOFs, characterized by their high surface area, tunable porosity, and structural diversity, serve as an excellent platform for the incorporation of lanthanides. Recent studies have shown that lanthanide doping modifies the band gap of MOFs, enhances visible light absorption, and facilitates the transfer of photogenerated carriers, thereby boosting the overall photocatalytic activity.[166,167] This subsection discusses the effects of doping lanthanide metals in MOFs on their stability and efficiency in PHE through water splitting.

In 2019, Huang *et al.* developed a new H_2BPDYC–Ce complex (UiO-67-Ce) by incorporating Ce(IV) into UiO-67 at a 0.02 Ce/Zr ratio and replaced the H_2BPDC ligands with H_2BPYDC. As a

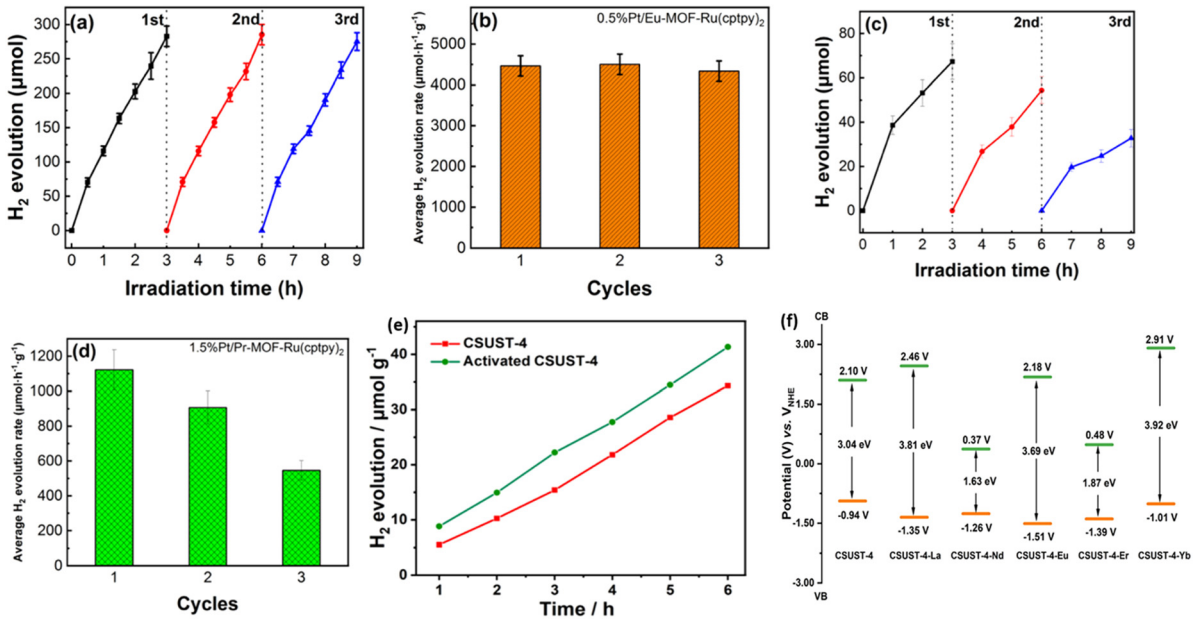

Fig. 7 (a) Photocatalytic H_2 production amounts in the cycle test and (b) the average rate of H_2 evolution during each cycle of 0.5% Pt/EuMOF-Ru(cptpy)$_2$. (c) Photocatalytic H_2 production amounts in the cycle test and (d) the average H_2 evolution rate during each cycle of 1.5% Pt/Pr-MOF-Ru(cptpy)$_2$. Reprinted with permission from ref. 164. Copyright 2023 ACS. (e) Time course of photocatalytic H_2 evolution of CSUST-4 and activated CSUST-4. (f) Energy diagrams of the HOMO and LUMO levels of CSUST-4 and CSUST-Ln (Ln = La, Nd, Eu, Er, Yb). Reprinted with permission from ref. 165. Copyright 2023 Wiley.

result, UiO-67-Ce exhibited a much higher PHE rate compared to UiO-67, with UiO-67-Ce achieving 269.6 μmol g^{-1} h^{-1}, which is more than ten times higher than UiO-67's rate of 26.78 μmol g^{-1} h^{-1} under identical experimental conditions. This significant enhancement in photocatalytic activity is attributed to the introduction of the Ce(IV) ion and the BPYDC-Ce ligand into the UiO-67 framework, which created new active sites and promoted efficient energy transfer processes. Despite this remarkable increase in activity under UV/Vis irradiation, neither UiO-67 nor UiO-67-Ce displayed any significant photocatalytic hydrogen production activity under visible light alone ($\lambda > 400$ nm), indicating that their performance is primarily driven by UV light (Fig. 8a). The ligand BPYDC-Ce displayed a much stronger UV intensity than BPDC, indicating that Ce coordinates with the N atoms in the ligand and not the carboxylate groups. An EPR signal with a *g*-value around 2.002, indicating Zr^{3+} formation *via* the LMCT process, is observed in both UiO-67-Ce and UiO-67. The signal is weaker in UiO-67-Ce, and no Zr^{3+} signal is detected in the dark for either material (Fig. 8b). This suggests that the LMCT process under UV/Vis light is reduced in UiO-67-Ce due to BPYDC-Ce. The introduction of BPYDC-Ce is said to weaken LMCT and promote energy transfer from BPDC to BPYDC-Ce, enhancing catalytic H_2 evolution.[168]

The stability of UiO-67-Ce during photocatalytic reactions was confirmed by consistent Ce/Zr ratios before and after testing, with no Ce ion leaching observed, indicating the catalyst maintained its structural integrity. However, after 6 hours of continuous UV/Vis irradiation, the H_2 evolution rate declined, suggesting reduced stability. XRD and SEM analyses revealed this decline was due to decreased crystallinity and morphological changes, with the cubic particles becoming irregular and larger. This structural degradation was likely caused by hydroxyl nucleophile attack and mechanical stress during the prolonged reaction.[168]

In the year 2022, Yang *et al.* studied the photocatalytic performance of a novel Ce-based MOF under visible light. The study presents the synthesis of a cerium-based metal–organic framework (Ce-MOF) named Ce-TBAPy using a solvothermal method. XRD confirmed its high crystallinity, showing Ce atoms coordinated with oxygen from the ligands. The material displayed a cubic morphology with strong Ce–O interactions, contributing to effective charge separation. Characterization techniques, including SEM, FT-IR, and NMR, revealed uniform elemental distribution and high thermal stability. XPS analysis showed a high concentration of Ce^{3+}, linked to oxygen vacancies that enhance photocatalytic performance (Fig. 8c and d). UV-Vis DRS indicated visible light absorption at 406 nm, with a band gap of 2.75 eV. The material demonstrated efficient electron–hole pair separation and improved photoreduction performance, particularly after loading a Pt co-catalyst. DFT calculations confirmed that the –COO–Ce functional groups facilitate electron transfer and inhibit recombination, boosting photocatalytic efficiency.

In terms of photocatalytic performance, Ce-TBAPy demonstrated exceptional hydrogen production under visible light irradiation, achieving hydrogen evolution 3.94 times higher than that of the untreated ligand (Fig. 8e). The material maintained its activity after three rounds of testing, indicating excellent recyclability and stability (Fig. 8f). The bandgap value

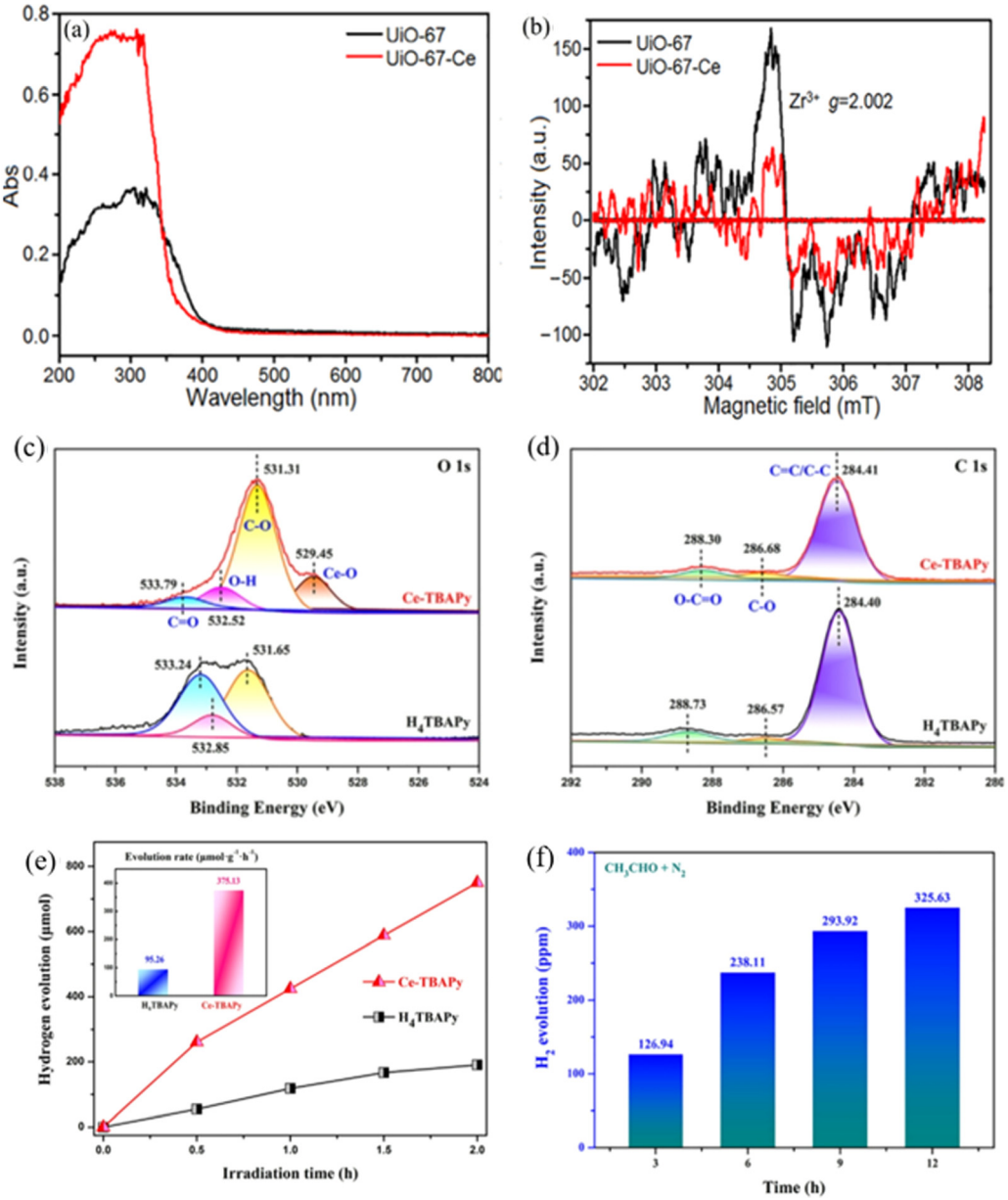

Fig. 8 (a) UV/Vis DRS of UiO-67 and UiO-67-Ce and (b) EPR spectra of UiO-67 and UiO-67-Ce in the presence of UV/Vis illumination. Reprinted with permission from ref. 168. Copyright 2019 Elsevier. High-resolution and separated peak curve XPS spectra of (c) O 1s and (d) C 1s. (e) Collaborative photocatalytic performance of H_2 liberation over Pt-loaded Ce-TBAPy in the CH_3CHO system under an N_2 atmosphere. (f) Time course of H_2 liberation and evolution rate curve (inset) of samples. Reprinted with permission from ref. 169. Copyright 2022 Elsevier.

of Ce-TBAPy (2.75 eV) and its conduction and VB positions made it well-suited for water reduction, with efficient electron transfer facilitated by the Pt co-catalyst. The overlapping structure of polycyclic aromatic conjugated polymers in the ligand further promoted rapid migration of photo-induced electrons, contributing to the overall efficiency of the photocatalytic process.[169]

4.3. Dye-like MOFs

Given the advancements in light-harvesting MOFs, integrating organic dyes or dye-like ligands as linkers in the construction of MOFs is a promising strategy. This leads to efficient light sensitization and an increased number of photocatalytic sites within a single structure, enhancing the MOF's photoactivity, stability, and insolubility. This approach simplifies the system by eliminating the need for complex electron relay systems and co-catalysts, making the MOF more effective at capturing and utilizing light.[170–174] The following section delves into the PHE performance of dye-like MOFs containing lanthanide metals.

An organic dye-like MOF was reported by X. Sun *et al.* for the first time in 2015, where 3,3′,5,5′-azobenzene tetracarboxylic acid was used as a linker in a Gd-MOF loaded with Ag nanoparticles. The framework was found to be stable in the pH range of 3 to 14 for up to 48 h. UV-Vis spectroscopy and

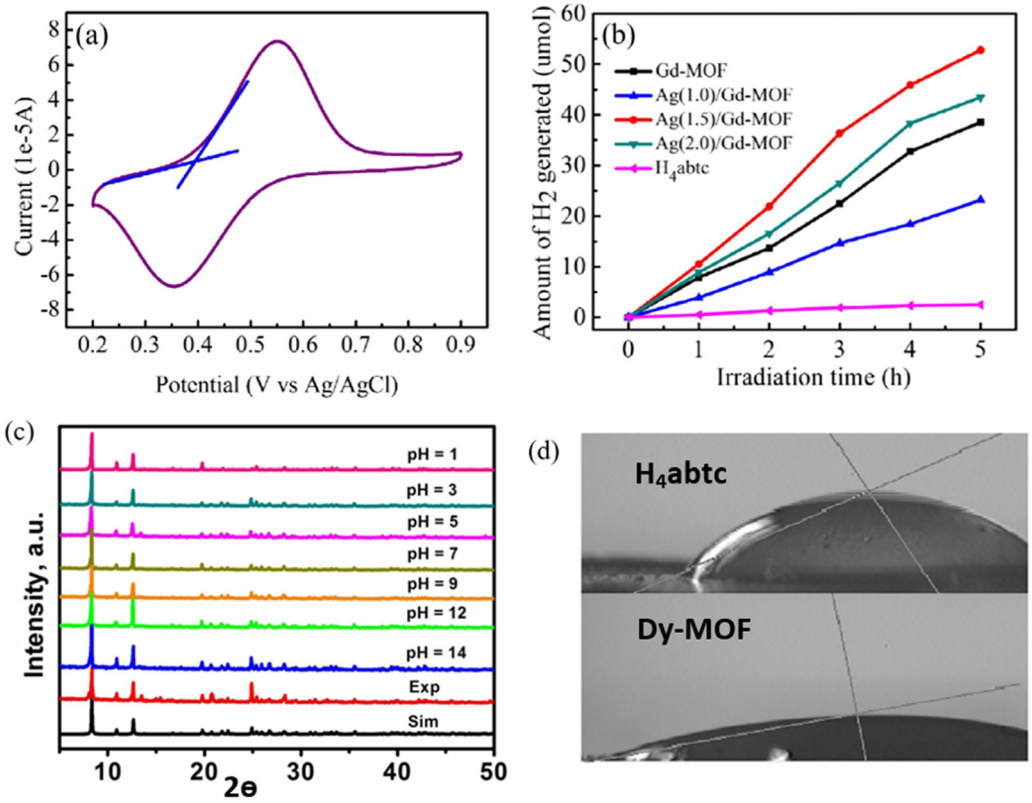

Fig. 9 (a) CV curves of the Gd-MOF. (b) Photocatalytic H_2 production under UV-Vis light irradiation over H_4abtc, Gd-MOF and Ag(X)/Gd-MOF. Reprinted with permission from ref. 175. (c) The pH stability of the dye-based Dy-MOF. (d) The differences in hydrophilicity between the dye-based Dy-MOF and H_4abtc ligand using contact angle measurements. Reprinted with permission from ref. 176. Copyright 2015 Royal Society of Chemistry.

electrochemical analysis revealed a broad absorption band and a favorable energy gap (2.35 eV) for photocatalytic activity. The solid-state cyclic voltammetry showed a suitable redox potential for proton reduction, confirming the potential of the MOF for hydrogen production (Fig. 9a).

In photocatalytic tests, the Gd-MOF produced H_2 at a rate of 7.71 μmol h^{-1} g^{-1} under UV-Vis light without a co-catalyst, comparable to that of UiO-66. Adding Ag as a co-catalyst significantly enhanced the performance. The Ag-loaded Gd-MOF (1.5 wt%) achieved a hydrogen production rate of 10.6 μmol h^{-1} g^{-1}, about 1.5 times higher than that of the Gd-MOF alone (Fig. 9b). This improvement is due to the role of Ag in enhancing charge separation and light absorption through surface plasmon resonance. The photocatalytic activity is maintained even after 5 hours of reaction, and the structure remains stable as confirmed by XRD. The electrochemical impedance spectra and luminescence studies further support the enhanced charge transfer and reduced recombination rates with Ag, leading to superior photocatalytic performance.[175]

In another similar work in 2018, Yu *et al.* synthesized a dye-based Dy-MOF through the reaction of $DyCl_3{\cdot}6H_2O$ and Na_4abtc. The crystal structure, determined *via* X-ray analysis, exhibits a novel 3D monoclinic framework with dimensions accommodating water channels. The dye-based Dy-MOF demonstrates impressive photocatalytic performance and stability. Under UV-Vis light irradiation, it achieves a high hydrogen production amount of 107.65 μmol g^{-1} over 5 hours, equivalent to 21.53 μmol g^{-1} h^{-1}. This rate surpasses that of many MOF-based catalysts without dye-like ligands, such as UiO-66 and ZIF-8, though it is somewhat lower compared to some porphyrin-based MOFs. The enhanced photocatalytic efficiency of the Dy-MOF is attributed to the inclusion of the dye-like ligand (H_4abtc), which significantly improves the light-harvesting capability. The UV-Vis absorption spectrum of the Dy-MOF shows broad light absorption with an edge above 570 nm, corresponding to a π–π* transition in organic ligands, indicating effective light capture. Additionally, the incorporation of 0.8% Ag as a co-catalyst markedly boosts activity. The Ag acts as an electron collector, enhancing charge separation and reducing electron–hole recombination, which further increases the hydrogen production rate. In terms of stability, the dye-based Dy-MOF exhibits robust thermal stability, maintaining its structural integrity up to 400 °C before collapsing, indicating its suitability for typical photocatalytic conditions.[176]

Furthermore, the material demonstrates excellent water stability, retaining its structural characteristics when soaked in solutions with pH values ranging from 3 to 14 for 48 h (Fig. 9c). This broad pH stability is essential for practical photocatalytic applications. Cycling tests reveal that the Dy-MOF maintains consistent hydrogen production performance up to the third cycle, with no significant loss of activity. Post-reaction analysis by X-ray diffraction (XRD) and FT-IR confirms

that the material's structure remains largely unchanged, underscoring its durability. Additionally, the Dy-MOF's lower contact angle of 21.5°, compared to 57.0° for the H_4abtc ligand, indicates higher hydrophilicity (Fig. 9d). This increased hydrophilicity enhances water adsorption, which is beneficial for efficient proton reduction during photocatalysis.[176]

4.4. Composites

Studies suggest that coupling MOFs with a catalytic semiconductor results in an efficient separation of charges and leads to an increase in the rate of H_2 evolution.[177] $ZnIn_2S_4$ (ZIS) based catalysts have an ability to absorb a broad spectrum of light (especially responsive to visible light), maintain structural and functional integrity over a prolonged period and have a tunable band gap energy that makes them suitable for application such as hydrogen production through water splitting.[178,179] However, electron–hole recombination occurs to a large extent in this material and in order to overcome this limitation various modifications are done by forming composites with other metal oxides and sulfides.[179–182] In this context, ZIS decorated with an Ln-MOF and Pt nanoparticles was reported in 2022 and its catalytic activity in water splitting was studied.[183] The SBUs comprising Tm and Gd were linked *via* 1,3,5-benzenetricarboxylic acid (BTC). The effect of the Ln-MOF in overall catalytic activity was studied by varying their % weight (1%, 5% and 10%). The ZIS spheres were clustered on the MOF microrods, making the arrangement suitable for electron transfer. The photo-deposition of Pt nanoparticles along with ZIS/(Tm,Gd)-BTC caused a significant increase in the lower wavelengths of the visible region.[183]

Increasing the % weight of the MOF in the ZIS composite showed a decrease in the intensity of photoluminescence, while ZIS/1% (Tm,Gd)-BTC/Pt exhibited the highest intensity of luminescence among the samples analyzed. Pt nanoparticles were shown to decrease the rate of recombination and thus the photoluminescence; however, the addition of (Tm, Gd)-BTC had only a minimal effect in decreasing the luminescence, suggesting a complex interplay in the luminescence behaviour (Fig. 10a). Partial decomposition of ZIS and loss of Pt were observed post-reaction through XRD and XPS studies. The efficiency of catalytic hydrogen generation was analysed using various samples in the aqueous solution of Na_2SO_3 and Na_2S (sacrificial electron donors). The samples used were pure ZIS, ZIS/Pt, ZIS/*x*% (Tm,Gd)-BTC and ZIS/*x*% (Tm,Gd)-BTC/Pt. Pure ZIS and ZIS modified with (Tm,Gd)-BTC at 1%, 5% and 10% by weight showed no activity in hydrogen generation, while the samples with Pt (ZIS/Pt and ZIS/*x*% (Tm,Gd)-BTC/Pt) were active in hydrogen production. ZIS modified with 1% (Tm,Gd)-BTC/Pt produced hydrogen at a rate of 1945.5 μmol g^{-1} h^{-1} when irradiated with UV-Vis light, which is much higher than that of pure ZIS,

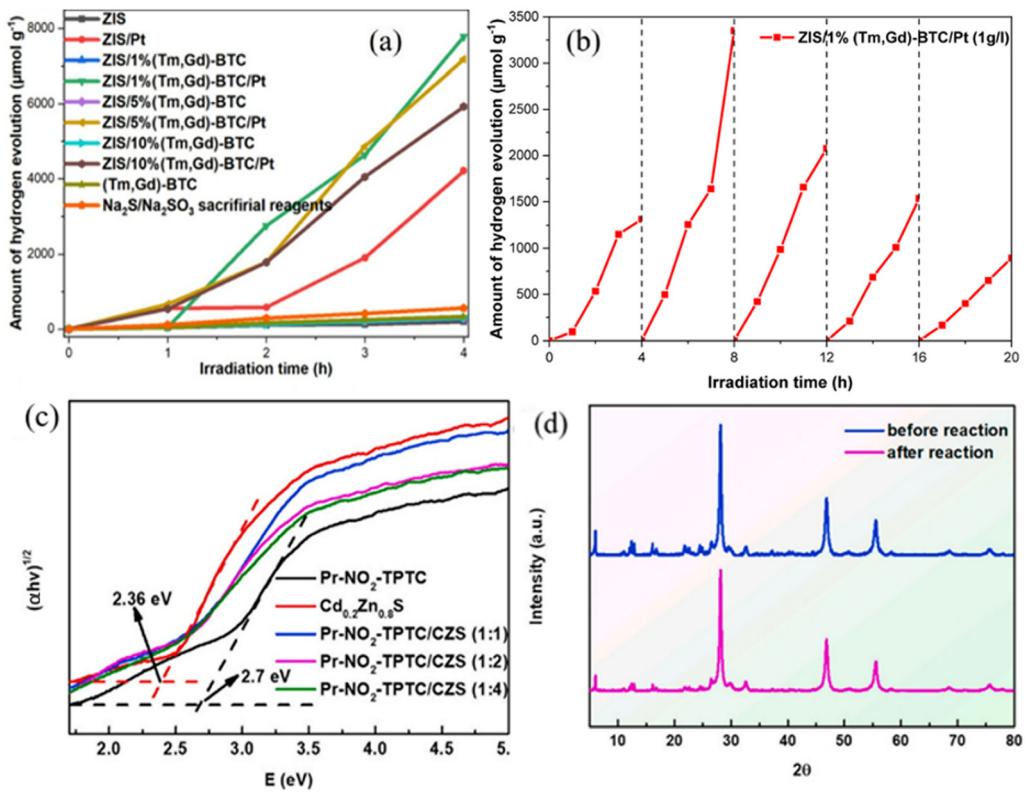

Fig. 10 (a) Amount of hydrogen produced for all obtained samples under UV-Vis irradiation (photocatalyst concentration: 1.25 g L^{-1}) and (b) amount of hydrogen produced in five photocatalytic cycles for ZIS/1% (Tm,Gd)-BTC/Pt (1 g L^{-1}) under visible light irradiation ($\lambda > 420$ nm). Reprinted with permission from ref. 183. (c) Photonic energy map of the photocatalysts. (d) PXRD patterns of Pr–NO_2–TPTC/CZS (1 : 1) before and after the photocatalytic reaction. Reprinted with permission from ref. 184. Copyright 2024 Elsevier.

which produced 49.07 μmol g^{-1} h^{-1}. Increasing the amount of the Ln-MOF, however, decreased the photoactivity of the sample. The highest hydrogen production rate was observed in the presence of both the MOF and the Pt NPs, *i.e.*, for 1 g L^{-1} ZIS/1% (Tm,Gd)-BTC/Pt where it produced a maximum of 2975 μmol g^{-1} h^{-1} of hydrogen when irradiated with UV-Vis. However, under visible light irradiation, its efficiency decreased as it produced only 328.17 μmol g^{-1} h^{-1} of hydrogen, which is lower than that of ZIS/Pt which produced 608.32 μmol g^{-1} h^{-1}. When tested for stability, ZIS/1% (Tm,Gd)-BTC/Pt displayed the highest efficiency in the second cycle, producing 837 μmol g^{-1} h^{-1} of hydrogen under visible light (Fig. 10b). The efficiency is said to decrease in the subsequent cycles.[183]

Since ZIS semiconductors face challenges such as low solar utilization, rapid recombination of carrier charges, and low quantum yields, binary metal sulfides such as $Cd_xZn_{1-x}S$, especially $Cd_{0.2}Zn_{0.8}S$, have shown promising stability, excellent carrier transport capacity, and adjustable band structure. $Cd_{0.2}Zn_{0.8}S$ has been identified to have the highest photocatalytic activity among different compositions of $Cd_xZn_{1-x}S$;[185] however, its application is limited because of the low separation and migration ability of photogenerated electron–hole pairs.

Recently, in 2024, a study by T.-T. Li *et al.* investigated the catalytic performance of $Cd_{0.2}Zn_{0.8}S$/Pr–NO_2–TPTC. The lanthanide MOF comprises binuclear clusters $[Pr_2(COO)_4]$ connected by multiple NO_2–$TPTC^{4-}$ ligands, creating a three-dimensional coordination framework. The NO_2–$TPTC^{4-}$ ligands are said to form hydrogen bonds with the lattice water in the solvent channels of the framework, thus enhancing absorption capacity and promoting water splitting to improve catalytic hydrogen production. The UV-Vis DRS shows absorption bands for Pr–NO_2–TPTC around 450 nm and for $Cd_{0.2}Zn_{0.8}S$ around 500 nm. When combining the Pr–NO_2–TPTC and the $Cd_{0.2}Zn_{0.8}S$ in various ratios, especially with a higher percentage of Pr–NO_2–TPTC, a red shift in the absorption peak is seen, indicating improved light absorption and narrower band gap width.[184]

Pristine Pr–NO_2–TPTC shows no catalytic performance; however, pure $Cd_{0.2}Zn_{0.8}S$ produces 2712 μmol g^{-1} h^{-1} of hydrogen. The composite Pr–NO_2–TPTC/CZS in a 1 : 1 ratio achieves the highest hydrogen production rate of 6321 μmol g^{-1} h^{-1}, which is 2.33 times higher than that of pure $Cd_{0.2}Zn_{0.8}S$. Other ratios, namely, 2 : 1 and 4 : 1, showed lower rates of hydrogen generation. The photonic energy map of the compounds is shown in Fig. 10c. The rate of hydrogen produced by $Cd_{0.2}Zn_{0.8}S$ was found to be 2092 μmol g^{-1} h^{-1} under visible light. Pr–NO_2–TPTC/CZS in a 1 : 1 ratio produced a slightly lower but still significant amount of hydrogen under visible light (5777 μmol g^{-1} h^{-1}). The catalytic performance of Pr–NO_2–TPTC/CZS (1 : 1) was maintained for three consecutive cycles, and there was no significant deterioration of the materials seen (Fig. 10d). The Mott–Schottky analysis revealed a positive slope indicating that the material is of n-type. In the photoluminescence studies, the weakest emission at 560 nm, which corresponded to Pr–NO_2–TPTC/CZS(1 : 1), showed a low extent of electron–hole recombination. The transient photocurrent experiments displayed a high response for the material, suggesting enhanced separation of photogenerated carriers. The material also presented reduced charge transfer resistance according to EIS. A heterojunction is said to form between $Cd_{0.2}Zn_{0.8}S$ and Pr–NO_2–TPTC, which promotes separation of the photogenerated charges and prolongs the carrier lifetime. UV-Vis light irradiation of both Pr–NO_2–TPTC and $Cd_{0.2}Zn_{0.8}S$ leads to the generation of electron–hole pairs. The electrons from the LUMO of Pr–NO_2–TPTC migrates to the CB of $Cd_{0.2}Zn_{0.8}S$, thus reducing H^+ in the water to produce hydrogen. While the holes move from the VB of $Cd_{0.2}Zn_{0.8}S$ to the HOMO of Pr–NO_2–TPTC and are consumed by the sacrificial agents (Na_2S and Na_2SO_3) present in the medium. The heterojunction that is present in this composite inhibits electron–hole recombination, and hence there are a greater number of electrons available for the reduction of protons.[184]

4.5. Derivatives

It is an interesting fact that MOFs can also act as sacrificial templates, which can then be converted into target multicomponent nanomaterials that serve as active photocatalysts. This section throws light on how catalysts derived from Ln-MOFs perform in PHE reactions, providing a clear insight on their efficiency and stability. For the first time, in 2019, Ce-doped g-C_3N_4 was reported, which was synthesized from MOFs made of Ti^{4+}, Zr^{4+}, Ce^{3+}, and Er^{3+} and then doped with four different amounts of Ce^{3+}, denoted as *x*Ce–C_3N_4 (*x* = 0.010, 0.015, 0.030, and 0.090 mol). Ce–C_3N_4 was modified using NH_4F, $NaHCO_3$, or cellulose acetate, producing NF-CN (NH_4F-modified), NHC-CN ($NaHCO_3$-modified), and CA-CN (cellulose acetate-modified) Ce–C_3N_4. Among the various Ce^{3+} concentrations tested, Ce–C_3N_4 with 0.015 mol Ce^{3+} exhibited the highest photocatalytic activity. This can be attributed to the optimal doping level of Ce^{3+}, which enhances the photocatalytic performance without causing excessive amorphization or disrupting the C_3N_4 lattice. At this concentration, Ce^{3+} effectively reduces the bandgap energy and enhances the separation efficiency of photoexcited electron–hole pairs. This leads to a more efficient photocatalytic process, as evidenced by the highest hydrogen production rates observed. In contrast, higher concentrations of Ce^{3+} (0.030 and 0.090 mol) result in decreased photocatalytic activity. This decline is due to the interference with the formation of the C_3N_4 structure and the introduction of excessive amorphous phases, which negatively impacts the material's ability to absorb light and facilitate charge separation.[186]

The sample demonstrates excellent stability under visible light irradiation for over 24 h across four cycles (Fig. 11a). The slight decrease in activity is due to TEOA consumption. Overall, 0.015Ce–C_3N_4 shows robust and consistent performance, making it suitable for practical applications. The modifications using $NaHCO_3$ and cellulose acetate also lead to significant improvements in photocatalytic activity. Cellulose acetate-modified samples, in particular, exhibit increased visible light absorption and better light-harvesting efficiency, contributing to improved photocatalytic performance. On the other hand, the incorporation of fluorine shifts both the VB and CB to

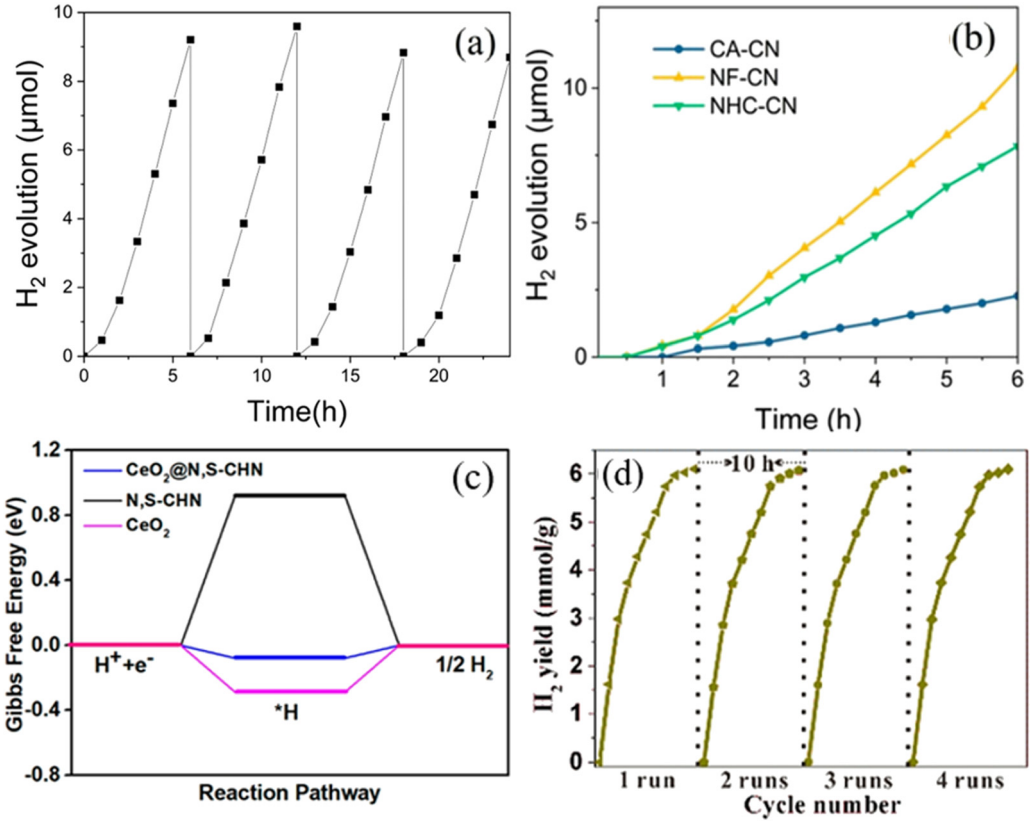

Fig. 11 (a) The 24 h cycling measurement of H_2 evolution from 0.015Ce–C_3N_4. (b) Photocatalytic H_2 evolution of CA-CN, NF-CN, and NHC-CN. Reprinted with permission from ref. 184. Copyright 2019 MDPI. (c) Gibbs free energy profile of the hydrogen evolution reaction for CeO_2@N,S–C HN (blue), N,S–C (black), and CeO_2 with the (111) crystal plane (pink). (d) The 40 h cycling measurement of H_2 evolution from CeO_2@N,S–C HN. Reprinted with permission from ref. 184. Copyright 2019 ACS.

higher energy levels, which enhances the photocatalytic activity by improving charge carrier dynamics (Fig. 11b). The stability of modified samples, including those doped with NH_4F, $NaHCO_3$, and cellulose acetate, aligns with the trends seen in base Ce–C_3N_4. These modifications generally enhance morphological stability, with NH_4F creating finer fibres and cellulose acetate and $NaHCO_3$ improving structural robustness. Consequently, these modifications contribute to more consistent and reliable photocatalytic activity[186].

In the following year, Hao *et al.* successfully synthesized N,S-codoped C-encapsulated CeO_2 with a hinge-like structure through the thermal decomposition of sulfanilic acid-modified Ce-based MOFs. The CeO_2@N,S–C HN catalyst demonstrated outstanding photocatalytic performance in PHE reactions. Its mass-normalized hydrogen production rate reached 555 μmol h^{-1} g^{-1}, surpassing those of CeO_2@C HN (405 μmol h^{-1} g^{-1}), CeO_2 HN (325 μmol h^{-1} g^{-1}), and commercial CeO_2 (195 μmol h^{-1} g^{-1}). The Gibbs free energy profile of the PHE reaction for all three compounds is given in Fig. 11c. This exceptional activity is largely due to the combination of the N,S-codoped carbon layer and the hinge-like porous structure of the catalyst. The N,S-codoped carbon enhances visible light absorption and facilitates efficient separation and transport of photogenerated charge carriers. The hinge-like structure further improves light trapping and enhances the photocatalytic process by allowing multiple reflections and increasing the interaction surface. Regarding stability, CeO_2@N,S–C HN exhibited impressive performance consistency over multiple cycles (Fig. 11d). In PHE tests under simulated sunlight irradiation, the catalyst maintained high activity over four cycles, with no significant loss in performance.

The stability was assessed through repeated cycling, and the catalyst showed negligible deactivation, maintaining its structural and compositional integrity throughout. Characterization techniques, such as XRD, SEM, and EDX, confirmed that the catalyst retained its morphology and elemental distribution after several cycles. This robust stability is attributed to the effective encapsulation of CeO_2 nanoparticles by the N,S-doped carbon layer, which protects the core material from degradation and preserves its catalytic properties over extended use. Overall, the CeO_2@N,S–C HN catalyst combines high photocatalytic efficiency with long-term stability, making it a promising candidate for sustainable photocatalytic applications.[187]

4.6. Photosensitizers

It is interesting that Ln-MOFs find application as photosensitizers in addition to all the aforementioned applications in PHE. This section summarizes the use of Ln-MOFs as

photosensitizers in aiding the production of hydrogen through water splitting. In a 2016 study by P. Wu *et al.*, the photosensitizing properties of a Gd-MOF featuring the TCA^{3-} ligand were extensively explored. The Gd-TCA framework benefits from the unique characteristics of Gd(III), which avoids unwanted energy transfer due to its lack of low energy levels below 32 000 cm^{-1}. This makes it particularly suited for photosensitizing applications. The framework's large surface area and porous structure enhance its stability and longevity in aqueous environments, facilitating processes such as hydrogen evolution. The UV-Vis spectrum of Gd-TCA shows a significant π–π^* transition at 350 nm, while its redox potentials are 0.82 V in the ground state and −2.30 V in the excited state. This indicates a strong capacity for electron transfer, crucial for effective hydrogen production. The study assessed the framework's performance with two different catalytic systems: an [Fe–Fe]-based hydrogenase mimic (C1) and a cobalt complex, $[Co(bpy)_3]Cl_2$ (C2).

For the [Fe–Fe]-based catalyst (C1), the addition of $NiPr_2EtH{\cdot}OAc$ as a sacrificial electron donor led to increased hydrogen production rates with higher catalyst concentrations. Initially, hydrogen production rates showed first-order dependence on C1 concentration (Fig. 12a), but this linear increase stalled at concentrations above 10 mM due to the poor solubility of C1. After 6 hours of irradiation, a notable drop in hydrogen production indicated potential decomposition of a system component. However, reintroducing C1 and $NiPr_2EtH{\cdot}OAc$ to the filtered MOF successfully resumed hydrogen production. Over a 40-hour period with four rounds of continuous irradiation, a total of 15 mL of hydrogen was produced. In contrast, the cobalt-based catalyst $[Co(bpy)_3]Cl_2$ (C2) demonstrated significant quenching of the emission of Gd-TCA but showed notable catalytic activity. Under alkaline conditions, Gd-TCA with C2 achieved a turnover frequency of 320 h^{-1} per molecule of C2 within the first hour and a quantum yield of 0.21%. While the hydrogen evolution rate increased with C2 concentration up to 50 μM, further increases did not enhance the rate linearly, likely due to catalyst decomposition (Fig. 12b). As with C1, the system's activity was restored with the addition of fresh C2 and base. This system also demonstrated impressive longevity, producing 22 mL of hydrogen over 20 hours and five rounds.

Additionally, Gd-TCA was utilized in the form of films supported by α-Al_2O_3, known for its high affinity towards carboxylic groups. The initial hydrogen production rate from a 1.5 × 0.5 cm^2 film was 1.71 mL h^{-1}, yielding 3.8 mL of

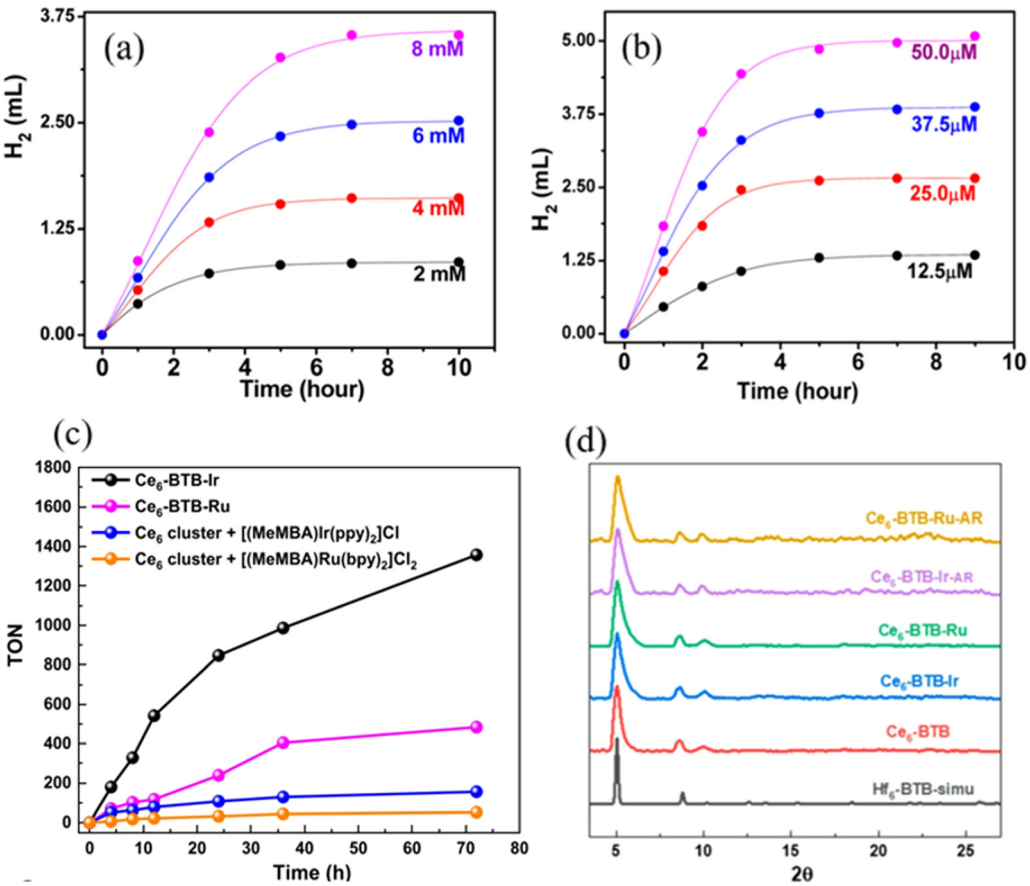

Fig. 12 (a) H_2 evolution of Gd-TCA (1 mg) in 5 mL of solution containing $NiPr_2EtH{\cdot}OAc$ (0.8 M) and C1 with various concentrations. (b) H_2 evolution of Gd-TCA (1 mg) in 5 mL of a solution containing Et_3N (2.5%) and C2 ($[Co(bpy)_3]Cl_2$) with various concentrations. Reprinted with permission from ref. 188. Copyright 2016 ACS. (c) Time-dependent PHE TONs of Ce_6-BTB-Ir and Ce_6-BTB-Ru along with homogeneous controls. (d) PXRD patterns of Ce_6-BTB (red), Ce_6-BTB-Ir (blue), Ce_6-BTB-Ru (green), and Ce_6-BTB-Ir after reaction (purple), and Ce_6-BTB-Ir after reaction (khaki) in comparison to that simulated for Hf6-BTB MOL (black). Reprinted with permission from ref. 134. Copyright 2020 ACS.

Table 3 Summary of Ln-MOFs and their derivatives discussed in this review

S. no.	Ln-MOF photocatalyst	Surface area of catalyst ($m^2\ g^{-1}$)	SDs and their concentration	Light sources	PHE rate ($\mu mol\ g^{-1}\ h^{-1}$)	TON	AQE	Stability	Ref.
1	UiO-66(Ce/Zr/Ti)	1019	Methanol	150 mW cm^{-2} Xe lamp ($\lambda > 450$ nm)	17.7 $\mu mol\ g^{-1}$	—	5.5%	Stable up to 2 cycles	157
2	0.5%Pt/Eu-MOF-Ru(cptpy)$_2$	4.0	AA (0.1 M)	300 W Xe lamp ($\lambda \geq 420$ nm)	4373 $\mu mol\ g^{-1}$	—	0.79%	Stable up to 3 cycles (9 h)	164
3	1.5%Pt/Pr-MOF-Ru(cptpy)$_2$	9.9	AA (0.1 M)	300 W Xe lamp ($\lambda \geq 420$ nm)	1047 $\mu mol\ g^{-1}$	—	—	Not very stable (3 h)	164
4	CSUST-4-Nd	—	TEOA (0.65 M)	300 W Xe lamp	71 $\mu mol\ g^{-1}$	—	—	Moderate thermal stability (up to 350 °C)	165
5	CSUST-4-Er	—	TEOA (0.65 M)	300 W Xe lamp	61 $\mu mol\ g^{-1}$	—	—		165
6	Activated CSUST-4	—	TEOA (0.65 M)	300 W Xe lamp	41 $\mu mol\ g^{-1}$	—	—		165
7	UiO-67-Ce	1545	Methanol	300 W Xe lamp	269.6 $\mu mol\ g^{-1}$	—	—	Stable up to 6 h	168
8	Ce-TBAPy	—	TEOA (0.65 M)	300 W Xe lamp ($\lambda \geq 420$ nm)	375.1 $\mu mol\ g^{-1}$	—	—	Good stability and recyclability up to 12 h	169
7	Ag(1.5)/Gd-ABTC	—	TEOA (~3 M)	300 W Xe lamp	10.6 $\mu mol\ g^{-1}$	—	—	Stable for 48 h at pH 3–14	175
8	0.8Pt/Dy-ABTC	—	TEOA (2.26 M)	300 W Xe lamp ($\lambda > 320$ nm)	21.5 $\mu mol\ g^{-1}$	—	—		176
9	ZIS/1% (Tm,Gd)-BTC/Pt	—	Na_2SO_3/Na_2S (0.25 M)	300 W Xe lamp ($\lambda \geq 420$ nm)	1945.5 $\mu mol\ g^{-1}$	—	—	Poor stability	183
10	Pr–NO_2–TPTC/*CZS* (1 : 1)	3.4480	Na_2SO_3/Na_2S	Full light	6321 $\mu mol\ g^{-1}$	—	—	Stable up to 12 h	184
11	CeO_2@N,S-C HN	26.9	—	Full light	555 $\mu mol\ g^{-1}$	—	—	Good stability up to 40 h	186
12	Gd-TCA/C1	—	$Nipr_2EtH{\cdot}OAc$ (0.8 M)	500 W Xe lamp	16.7 $\mu mol\ g^{-1}$	—	—	Poor stability	188
13	Gd-TCA/C2	—	Et_3N (0.179 M)	500 W Xe lamp	49.1 $\mu mol\ g^{-1}$	—	0.21%	Poor stability	188
14	Gd-TCA film	—	Et_3N (0.179 M)	500 W Xe lamp	76.3 $\mu mol\ g^{-1}$	—	—	Stable up to 40 h	188
15	Ce_6-BTB-Ir	—	BIH	13.9 W 350–700 nm solid-state plasma light source	—	1357	4.8%	Good stability	134
16	Ce_6-BTB-Ru	—	BIH	13.9 W 350–700 nm solid-state plasma light source	—	484	3.8%	Good stability	134

hydrogen in the first 5 hours under alkaline conditions with 50 μM C2. The film-based system maintained hydrogen production for over 40 hours, generating a total of 33.5 mL of hydrogen. This study marks the first reported use of MOF films for the photochemical reduction of water, highlighting the exceptional performance and stability of Gd-TCA framework in both powder and film forms.[188]

In addressing the limitations of traditional MOFs in photocatalysis, such as light scattering at the nanoscale and inefficient light penetration in bulk forms, researchers have developed metal–organic layers (MOLs). MOLs, as monolayer versions of MOFs, offer improved photocatalytic performance by reducing light scattering and enhancing diffusion of reaction components. This innovation aims to overcome the constraints imposed by MOF symmetry and channel diffusion issues. The first Ce-based MOL was successfully synthesized and studied by Song *et al.* in 2020. The SBUs are made of Ce_6 clusters, and they are linked using BTB molecules.[134] The MOLs are capped with photosensitizing molecules such as $[(HMBA)Ir(ppy)_2]Cl$ and $[(HMBA)Ru(bpy)_2]Cl_2$. The study evaluates the PHE activities of two metal–organic layers (MOLs): Ce_6-BTB-Ir and Ce_6-BTB-Ru. These MOLs were tested in an oxygen-free acetonitrile solution with acetic acid as the proton source and 1,3-dimethyl-2-phenyl-2,3-dihydro-1*H*-benzo[*d*]imidazole (BIH) as the sacrificial agent. The performance was assessed by quantifying hydrogen production through gas chromatography. Both Ce_6-BTB-Ir and Ce_6-BTB-Ru exhibited impressive PHE activities, with turnover numbers (TONs) of 1357 and 484, respectively (Fig. 12c), following 72 hours of photoirradiation using a solid-state plasma light source. The apparent quantum yields were 4.8% for Ce_6-BTB-Ir and 3.8% for Ce_6-BTB-Ru. These results highlight the superior photocatalytic performance of these MOLs compared to their homogeneous counterparts, which demonstrated significantly lower TONs.[134]

Stability was a crucial aspect of the study. Both Ce_6-BTB-Ir and Ce_6-BTB-Ru maintained their structural integrity after PHE, as evidenced by consistent PXRD patterns (Fig. 12d) and HRTEM images, with less than 3% leaching of Ce into the solution. The MOLs also retained their photocatalytic activity over at least three consecutive runs, demonstrating their durability under reaction conditions. This structural stability and enduring activity underscore the effectiveness of MOLs in photocatalytic applications.[134]

The summary of all Ln-MOFs discussed above is given in Table 3. Apart from all these studies reported regarding the efficiency of Ln-MOFs in photocatalytic water-splitting processes, various computational studies suggest that Ln-MOFs are promising candidates to be employed in photocatalytic water-splitting. For instance, in 2020, Anderson *et al.* presented two series of lanthanide-based MOFs (Ln-SION1 and Ln-SION-2) and found that the Ln-SION1 series shows photoconductivity due to its desirable orbital structure. They conclude that the latter members of the series have the potential to act as photocatalysts for water-splitting, with the help of a photocatalyst.[189] Additionally, Hidalgo-Rosa *et al.*, in 2023, discussed the significance of functional groups on enhancing

the light-harvesting nature of rare earth MOFs and suggested that these materials could show photocatalytic properties upon solar light irradiation.[190] All these studies emphasize that numerous opportunities lie ahead of researchers in the field of photocatalytic water-splitting when it comes to lanthanide-based MOFs. Furthermore, their structural tunability and reusability align with the goals of sustainable hydrogen production. However, economic feasibility remains a significant challenge. The high cost of lanthanides, due to their scarcity and complex extraction processes, and the intricate synthesis methods required for Ln-MOFs make them expensive to produce. Scaling up production while maintaining performance is also challenging, further hindering their large-scale adoption. Additionally, these materials face competition from more cost-effective alternatives such as transition metal-based catalysts like TiO_2 or ZnO which are widely available and easy to produce. Real-world deployment of Ln-MOFs requires further validation of their efficiency and stability under practical conditions, as laboratory performance may not directly translate to operational environments. Despite these challenges, strategies such as materials optimization—using mixed-metal MOFs or doping to reduce lanthanide content—can lower costs while maintaining functionality. Advances in synthesis techniques, including greener and scalable methods, along with recycling and recovery of lanthanides from spent MOFs, could further enhance economic viability. As global demand for sustainable energy solutions grows, increased research and industrial collaboration may drive cost reductions and facilitate commercialization. Although currently less economically competitive, Ln-MOFs remain a promising avenue for green hydrogen production with further technological and economic advancements.

5. Conclusions and future outlook

Lanthanide-MOFs have emerged as promising materials for photocatalysis in recent years, particularly in hydrogen production *via* PHE. The unique properties of lanthanides, such as their distinctive luminescence and the ability to finely tune their electronic and optical characteristics, have driven significant advancements in this field. Early research on the luminescence of Ln-MOFs provided insights into energy transfer mechanisms, revealing how these frameworks harness light and convert it into usable energy, which is crucial for enhancing photocatalytic efficiency.

Ln-MOFs have gained significant attention in photocatalysis, particularly for hydrogen production *via* water splitting, due to their unique ability to form mixed-metal frameworks without altering the MOF structure. This flexibility is made possible by the similar crystal structures of adjacent rare earth ions, which allows for the introduction of active sites and the enhancement of catalytic performance through electron relay between different metal nodes. The result is a material that can be finely tuned for optimal photocatalytic efficiency. Recent advancements in the field have demonstrated that trimetallic Ln-MOFs, which integrate three different metals into a single framework, can achieve a significant boost in catalytic activity compared to their single-metal counterparts. This improvement is primarily due to the broader absorption spectrum and reduced band gap that these mixed-metal systems offer, enabling more efficient light harvesting and energy transfer. Additionally, lanthanide doping, particularly in combination with Pt co-catalysts, has proven to be an effective strategy for further enhancing the photocatalytic efficiency and stability of these materials. The introduction of Pt helps to improve charge separation and transfer, leading to more efficient hydrogen production. To overcome traditional limitations of MOFs, such as light scattering and inefficient light penetration, researchers have developed MOLs. These thinner materials, combined with photosensitizing molecules, exhibit high PHE activities while maintaining their structural integrity over multiple cycles. Gd-based Ln-MOFs have also shown promise in this area, demonstrating effective electron transfer and strong photocatalytic activity, resulting in sustained hydrogen production over extended periods. Ln-MOFs have also been used as sacrificial templates to create more efficient photocatalysts. These materials exhibit enhanced visible light absorption and charge separation, leading to superior photocatalytic activity and stability. Furthermore, the combination of Ln-MOFs with catalytic semiconductors has shown significant potential in further enhancing hydrogen production. Ln-MOF–semiconductor composites take advantage of the synergistic effects of both materials, resulting in improved light absorption, charge separation, and overall photocatalytic efficiency. In addition, numerous studies support the fact that lanthanide-based MOFs show efficient LMCT and upconversion properties. Nd based complexes and MOFs have shown photon upconversion properties through which they emit blue light.[191–193] Up-conversion displayed by lanthanides represents a powerful approach to enhance photocatalytic water-splitting.

Overall, incorporation of lanthanides into frameworks increases their photocatalytic activity, somewhere from 2.3 in UiO-67-Ce to 10 times in Pr–NO_2–TPTC/CZS (1 : 1), by altering their band gap values and hence improving light absorption. Among all the lanthanides discussed in this review, Ce, Eu, Pr, Tm and Gd outperform other lanthanides by improving charge separation and light absorption, owing to their unique electronic structure. Although almost all of the studies involve the use of SDs, Ce-doped g-CN seems to have performed the best in our opinion, exhibiting an excellent hydrogen production rate in the absence of an SD and appreciable stability up to 40 h; in addition to Ce-doped g-CN, Pr–NO_2–TPTC/CZS (1 : 1) and Eu-MOF-Ru(cptpy)$_2$ also offer notable efficiency and hence can be used in practical applications. The incorporation of dye-like ligands, multiple lanthanides, and semiconductors are indeed innovative approaches to enhance the PHE performance of Ln-MOFs.

With all this being said, future research on Ln-MOFs should focus on several key areas to fully unlock their potential in photocatalysis, particularly for hydrogen production. One critical area is enhancing the quantum efficiency of Ln-MOFs through optimizing photon absorption, energy transfer

processes, and minimizing non-radiative losses, which will be crucial for boosting the overall photocatalytic performance of these materials. Exploring new lanthanide elements and their combinations within MOFs is another promising avenue. Less commonly studied lanthanides could offer unique optical and electronic properties, potentially leading to improved band gaps and more efficient energy transfer mechanisms. The creation of mixed-metal MOFs, leveraging the identical crystal structures of adjacent lanthanide ions, allows for the introduction of active sites and enhances catalytic performance through electron relay between different metal nodes. The integration of Ln-MOFs with emerging technologies, such as artificial photosynthesis and solar fuel production, could open new avenues for clean energy applications. However, most of the Ln-MOFs still face challenges in effectively utilizing sunlight. Most of the Ln-MOFs reported derive their photocatalytic activity to a major extent from UV light that constitutes only about 5%. Hence the visible-light response of these catalysts has to be improved. Furthermore, improving the stability and durability of Ln-MOFs under prolonged irradiation and harsh reaction conditions remains a challenge. Future research should focus on developing more robust materials that maintain their performance over extended periods, addressing issues like structural degradation and the stability of doped and composite MOFs. Furthermore, with the advancements in artificial intelligence (AI) technologies, machine learning (ML) has become a great tool with vast applications. ML has the potential to revolutionize the design of Ln-MOFs for PHE. By rapidly predicting key properties such as band gaps, charge carrier mobility, and photocatalytic activity, ML models can accelerate the screening and optimization of Ln-MOFs. These models can be trained on existing data from quantum chemical calculations like density functional theory or experimental results, allowing researchers to explore vast compositional spaces and identify the most promising materials. By integrating ML with high-throughput experiments, materials synthesis, and computational chemistry, researchers can significantly reduce the time and cost involved in discovering and optimizing new Ln-MOFs for hydrogen production. This interdisciplinary approach fosters the development of high-performance photocatalysts, making ML an essential tool in advancing sustainable energy solutions. Finally, assessing the environmental and economic impacts of Ln-MOFs in large-scale applications will be crucial for ensuring their sustainability and informing their adoption in practical systems for energy and environmental applications. Developing frameworks resistant to hydrolytic and photochemical degradation will enhance stability. Replacing expensive co-catalysts like Pt with earth-abundant alternatives (*e.g.*, Ni, Co) is crucial for cost reduction. Research into dye-based MOFs and composites can improve visible-light activity, while scalable and cost-effective synthesis methods will facilitate the transition from lab-scale research to industrial applications. Continued research and development in this field, focusing on new materials, synthesis methods, and real-world applications, will be crucial for unlocking the full potential of Ln-MOFs and addressing global energy and environmental challenges.

Abbreviations

AA	Ascorbic acid
Ag	Silver
Al	Aluminium
AQE	Apparent quantum efficiency
ATA	2-Aminoterephthalate
Au	Gold
$BiVO_4$	Bismuth vanadate(v)
BPDC	Biphenyl-4,4′-dicarboxylic acid
Bpy	2,2′-Bipyridine
BPYDC	2,2′-Bipyridine-4,4′-dicarboxylate
BTC	Benzene-1,3,5-tricarboxylic acid
CB	Conduction band
CdS	Cadmium(II) sulfide
Ce	Cerium
CeO_2	Cerium(IV) oxide
$CH_3NH_3PbI_3$	Methylammonium lead iodide
CoPi	Cobalt phosphate
COF	Covalent organic framework
CPP	Conjugated porous polymer
CSUST	Changsha University of Science and Technology
Cu	Copper
Cu_2O	Copper(I) oxide
CZS	Cadmium zinc sulfide
$DyCl_3{\cdot}6H_2O$	Dysprosium(III) chloride
Eu	Europium
Fe_2O_3	Iron(III) oxide
Gd	Gadolinium
g-C_3N_4	Graphitic carbon nitride
H_3TCA	Taurocholic acid
H_4abtc	3,3′,5,5′-Azobenzene-tetracarboxylic acid
H_4TPTC	[1,1′:4′,1″]Terphenyl-3,3″,5,5″-tetracarboxylic acid
Hcptpy	4′-(4-Carboxyphenyl)-2,2′:6′,2″-terpyridine
HER	Hydrogen evolution reaction
HOMO	Highest occupied molecular orbital
La	Lanthanum
Ln	Lanthanide
Ln-MOFs	Lanthanide-metal–organic frameworks
LMCT	Ligand-to-metal charge transfer
LSPR	Localized surface plasmon resonance
LUMO	Lowest unoccupied molecular orbital
MIL	Materials of Institute Lavoisier
MOL	Metal–organic layer
MoS_2	Molybdenum(IV) sulfide
Na_2S	Sodium sulfide
Na_2SO_3	Sodium sulfite
NH_4F	Ammonium fluoride
Ni	Nickel
OER	Oxygen evolution reaction
PHE	Photocatalytic hydrogen evolution
Pr	Praseodymium
PS	Photosensitizer
Pt	Platinum

RE-MOFs	Rare earth metal–organic frameworks
RuO_x	Ruthenium oxide
SBU	Secondary building unit
SD	Sacrificial donor
Tb	Terbium
TBAPy	4,4′,4″-(Pyridine-2,4,6-triyl)tribenzaldehyde
TEOA	Triethanolamine
TiO_2	Titanium(IV) oxide
Tm	Thulium
VB	Valence band
WO_3	Tungsten(VI) oxide
Yb	Ytterbium
ZIS	Zinc indium sulfide
ZnO	Zinc(II) oxide

Author contributions

P. Danita Patricia: conceptualization, writing – original draft. Rajadurai Vijay Solomon: conceptualization, supervision, draft editing.

Data availability

Data sharing is not applicable to this review article as no new data were created or analyzed in this study.

Conflicts of interest

The authors declare that they have no competing interests.

Acknowledgements

P. Danita Patricia acknowledges the support of MCC-MRF Innovation Park, Madras Christian College, during her internship (May to August 2024) which contributed to the completion of this review. Dr R. Vijay Solomon acknowledges the support provided by the Department of Chemistry, Madras Christian College, Chennai.

References

1 J. A. Francis and S. J. Vavrus, Evidence linking Arctic amplification to extreme weather in mid-latitudes, *Geophys. Res. Lett.*, 2012, **39**, L06801.
2 C. Acar and I. Dincer, Review and evaluation of hydrogen production options for better environment, *J. Cleaner Prod.*, 2019, **218**, 835–849.
3 A. M. Abdalla, S. Hossain, O. B. Nisfindy, A. T. Azad, M. Dawood and A. K. Azad, Hydrogen production, storage, transportation and key challenges with applications: A review, *Energy Convers. Manage.*, 2018, **165**, 602–627.
4 C. Tarhan and M. A. Çil, A study on hydrogen, the clean energy of the future: Hydrogen storage methods, *J. Energy Storage*, 2021, **40**, 102676.
5 S. N. Reddy, S. Nanda, D. V. N. Vo, T. D. Nguyen, V. H. Nguyen and B. Abdullah, *et al.*, Hydrogen: fuel of the near future, in *New Dimensions in Production and Utilization of Hydrogen*, Elsevier, 2020, pp. 1–20.
6 Y. Bicer and I. Dincer, Life cycle evaluation of hydrogen and other potential fuels for aircrafts, *Int. J. Hydrogen Energy*, 2017, **42**(16), 10722–10738.
7 P. Chiesa, G. Lozza and L. Mazzocchi, Using Hydrogen as Gas Turbine Fuel, *J. Eng. Gas Turbines Power*, 2005, **127**(1), 73–80.
8 S. Szwaja and K. Grab-Rogalinski, Hydrogen combustion in a compression ignition diesel engine, *Int. J. Hydrogen Energy*, 2009, **34**(10), 4413–4421.
9 H. T. Arat, M. K. Baltacioglu, K. Aydin and M. Özcanli, Experimental investigation of using 30HCNG fuel mixture on a non-modified diesel engine operated with various diesel replacement rates, *Int. J. Hydrogen Energy*, 2016, **41**(4), 3199–3207.
10 M. R. Gogate, The direct dimethyl ether (DME) synthesis process from syngas I. Process feasibility and chemical synergy in one-step LPDME tm process, *Pet. Sci. Technol.*, 2018, **36**(8), 547–554.
11 P. P. Edwards, V. L. Kuznetsov, W. I. F. David and N. P. Brandon, Hydrogen and fuel cells: Towards a sustainable energy future, *Energy Policy*, 2008, **36**(12), 4356–4362.
12 M. Hermesmann and T. E. Müller, Green, Turquoise, Blue, or Grey? Environmentally friendly Hydrogen Production in Transforming Energy Systems, *Prog. Energy Combust. Sci.*, 2022, **90**, 100996.
13 M. Yu, K. Wang and H. Vredenburg, Insights into low-carbon hydrogen production methods: Green, blue and aqua hydrogen, *Int. J. Hydrogen Energy*, 2021, **46**(41), 21261–21273.
14 G. J. Stiegel and M. Ramezan, Hydrogen from coal gasification: An economical pathway to a sustainable energy future, *Int. J. Coal Geol.*, 2006, **65**(3–4), 173–190.
15 M. Y. Azwar, M. A. Hussain and A. K. Abdul-Wahab, Development of biohydrogen production by photobiological, fermentation and electrochemical processes: A review, *Renewable Sustainable Energy Rev.*, 2014, **31**, 158–173.
16 K. E. Lamb, M. D. Dolan and D. F. Kennedy, Ammonia for hydrogen storage; A review of catalytic ammonia decomposition and hydrogen separation and purification, *Int. J. Hydrogen Energy*, 2019, **44**(7), 3580–3593.
17 J. Yang, Z. Cui, J. Ma and Z. Dong, Ru coated Co nanoparticles decorated on cotton derived carbon fibers as a highly efficient and magnetically recyclable catalyst for hydrogen generation from ammonia borane, *Int. J. Hydrogen Energy*, 2018, **43**(3), 1355–1364.
18 J. D. Holladay, J. Hu, D. L. King and Y. Wang, An overview of hydrogen production technologies, *Catal. Today*, 2009, **139**(4), 244–260.
19 A. Steinfeld, Solar thermochemical production of hydrogen––a review, *Sol. Energy*, 2005, **78**(5), 603–615.
20 A. Gupta, B. Likozar, R. Jana, W. C. Chanu and M. K. Singh, A review of hydrogen production processes by

photocatalytic water splitting – From atomistic catalysis design to optimal reactor engineering, *Int. J. Hydrogen Energy*, 2022, **47**(78), 33282–33307.

21 M. Ji and J. Wang, Review and comparison of various hydrogen production methods based on costs and life cycle impact assessment indicators, *Int. J. Hydrogen Energy*, 2021, **46**(78), 38612–38635.

22 A. Ajanovic, M. Sayer and R. Haas, The economics and the environmental benignity of different colors of hydrogen, *Int. J. Hydrogen Energy*, 2022, **47**(57), 24136–24154.

23 D. M. F. Santos, C. A. C. Sequeira and J. L. Figueiredo, Hydrogen production by alkaline water electrolysis, *Quim. Nova*, 2013, **36**(8), 1176.

24 S. Y. Tee, K. Y. Win, W. S. Teo, L. Koh, S. Liu and C. P. Teng, *et al.*, Recent Progress in Energy-Driven Water Splitting, *Adv. Sci.*, 2017, **4**, 1600337.

25 S. Grigoriev, V. Porembsky and V. Fateev, Pure hydrogen production by PEM electrolysis for hydrogen energy, *Int. J. Hydrogen Energy*, 2006, **31**(2), 171–175.

26 J. Pettersson, B. Ramsey and D. Harrison, A review of the latest developments in electrodes for unitised regenerative polymer electrolyte fuel cells, *J. Power Sources*, 2006, **157**(1), 28–34.

27 T. Hisatomi, J. Kubota and K. Domen, Recent advances in semiconductors for photocatalytic and photoelectrochemical water splitting, *Chem. Soc. Rev.*, 2014, **43**(22), 7520–7535.

28 M. Ali, E. Pervaiz, T. Noor, O. Rabi, R. Zahra and M. Yang, Recent advancements in MOF-based catalysts for applications in electrochemical and photoelectrochemical water splitting: A review, *Int. J. Energy Res.*, 2021, **45**(2), 1190–1226.

29 A. Kudo and Y. Miseki, Heterogeneous photocatalyst materials for water splitting, *Chem. Soc. Rev.*, 2009, **38**(1), 253–278.

30 X. Li, J. Yu, J. Low, Y. Fang, J. Xiao and X. Chen, Engineering heterogeneous semiconductors for solar water splitting, *J. Mater. Chem. A*, 2015, **3**(6), 2485–2534.

31 S. Zhao, Y. Zhang, Y. Zhou, J. Fang, Y. Wang and C. Zhang, *et al.*, Fabrication of sandwich-structured g-C3N4/Au/BiOCl Z-scheme photocatalyst with enhanced photocatalytic performance under visible light irradiation, *J. Mater. Sci.*, 2018, **53**(8), 6008–6020.

32 J. Xiao, L. Han, J. Luo, S. Yu and H. Jiang, Integration of Plasmonic Effects and Schottky Junctions into Metal–Organic Framework Composites: Steering Charge Flow for Enhanced Visible-Light Photocatalysis, *Angew. Chem., Int. Ed.*, 2018, **57**(4), 1103–1107.

33 Y. Wu, P. Wang, X. Zhu, Q. Zhang, Z. Wang and Y. Liu, *et al.*, Composite of CH 3 NH 3 PbI 3 with Reduced Graphene Oxide as a Highly Efficient and Stable Visible-Light Photocatalyst for Hydrogen Evolution in Aqueous HI Solution, *Adv. Mater.*, 2018, **30**, 1704342.

34 X. Wang, H. Wang, H. Zhang, W. Yu, X. Wang and Y. Zhao, *et al.*, Dynamic Interaction between Methylammonium Lead Iodide and TiO_2 Nanocrystals Leads to Enhanced Photocatalytic H_2 Evolution from HI Splitting, *ACS Energy Lett.*, 2018, **3**(5), 1159–1164.

35 K. He, J. Xie, Z. Yang, R. Shen, Y. Fang and S. Ma, *et al.*, Earth-abundant WC nanoparticles as an active noble-metal-free co-catalyst for the highly boosted photocatalytic H_2 production over g-C_3N_4 nanosheets under visible light, *Catal. Sci. Technol.*, 2017, **7**(5), 1193–1202.

36 H. Chen, D. Jiang, Z. Sun, R. M. Irfan, L. Zhang and P. Du, Cobalt nitride as an efficient cocatalyst on CdS nanorods for enhanced photocatalytic hydrogen production in water, *Catal. Sci. Technol.*, 2017, **7**(7), 1515–1522.

37 A. Meng, L. Zhang, B. Cheng and J. Yu, Dual Cocatalysts in TiO 2 Photocatalysis, *Adv. Mater.*, 2019, **31**, 1807660.

38 J. Ran, J. Zhang, J. Yu, M. Jaroniec and S. Z. Qiao, Earth-abundant cocatalysts for semiconductor-based photocatalytic water splitting, *Chem. Soc. Rev.*, 2014, **43**(22), 7787–7812.

39 G. Knorr, K. Hotzel, A. Chettri, A. Skabeev, M. Wächtler and B. Dietzek-Ivanšić, *et al.*, Unlocking the potential of ketocoumarins: efficient photosensitizers for sustainable light driven hydrogen evolution, *J. Mater. Chem. A*, 2023, **11**(43), 23260–23269.

40 F. S. Khalkhali, E. Kowsari, S. Ramakrishna, M. Eqbalpour, M. Gheibi and H. Esmaili, A review on the photosensitizers used for enhancing the photoelectrochemical performance of hydrogen production with emphasis on a novel toxicity assessment framework, *Int. J. Hydrogen Energy*, 2024, **51**, 990–1022.

41 C. F. Leung and T. C. Lau, Organic Photosensitizers for Catalytic Solar Fuel Generation, *Energy Fuels*, 2021, **35**(23), 18888–18899.

42 E. Bassan, A. Gualandi, P. G. Cozzi and P. Ceroni, Design of BODIPY dyes as triplet photosensitizers: electronic properties tailored for solar energy conversion, photoredox catalysis and photodynamic therapy, *Chem. Sci.*, 2021, **12**(19), 6607–6628.

43 D. Kim, V. Q. Dang and T. S. Teets, Improved transition metal photosensitizers to drive advances in photocatalysis, *Chem. Sci.*, 2024, **15**(1), 77–94.

44 S. Rana, A. Kumar, P. Dhiman, G. Sharma, J. Amirian and F. J. Stadler, Progress in graphdiyne and phosphorene based composites and heterostructures as new age materials for photocatalytic hydrogen evolution, *Fuel*, 2024, **356**, 129630.

45 Q. Li, X. Li and J. Yu, Surface and interface modification strategies of CdS-based photocatalysts, *Interface Sci. Technol.*, 2020, **31**, 313–348.

46 S. Qiao, M. Di, J. X. Jiang and B. H. Han, Conjugated porous polymers for photocatalysis: The road from catalytic mechanism, molecular structure to advanced applications, *EnergyChem*, 2022, **4**(6), 100094.

47 M. A. Fox and T. L. Pettit, Photoactivity of zeolite-supported cadmium sulfide: hydrogen evolution in the presence of sacrificial donors, *Langmuir*, 1989, **5**(4), 1056.

48 A. Fujishima and K. Honda, Electrochemical Photolysis of Water at a Semiconductor Electrode, *Nature*, 1972, **238**(5358), 37–38.

49 C. G. Morales-Guio, L. Liardet and X. Hu, Oxidatively Electrodeposited Thin-Film Transition Metal (Oxy)hydroxides as Oxygen Evolution Catalysts, *J. Am. Chem. Soc.*, 2016, **138**(28), 8946–8957.
50 X. Xia, J. H. Pan, X. Pan, L. Hu, J. Yao and Y. Ding, *et al.*, Photochemical Conversion and Storage of Solar Energy, *ACS Energy Lett.*, 2019, **4**(2), 405–410.
51 L. Vayssieres, N. Beermann, S. E. Lindquist and A. Hagfeldt, Controlled Aqueous Chemical Growth of Oriented Three-Dimensional Crystalline Nanorod Arrays: Application to Iron(III) Oxides, *Chem. Mater.*, 2001, **13**(2), 233–235.
52 L. Trotochaud, S. L. Young, J. K. Ranney and S. W. Boettcher, Nickel–Iron Oxyhydroxide Oxygen-Evolution Electrocatalysts: The Role of Intentional and Incidental Iron Incorporation, *J. Am. Chem. Soc.*, 2014, **136**(18), 6744–6753.
53 A. Paracchino, V. Laporte, K. Sivula, M. Grätzel and E. Thimsen, Highly active oxide photocathode for photoelectrochemical water reduction, *Nat. Mater.*, 2011, **10**(6), 456–461.
54 R. Bajaj, M. Sharma and D. Bahadur, Visible light-driven novel nanocomposite ($BiVO_4/CuCr_2O_4$) for efficient degradation of organic dye, *Dalton Trans.*, 2013, **42**(19), 6736.
55 S. N. Frank and A. J. Bard, Heterogeneous photocatalytic oxidation of cyanide ion in aqueous solutions at titanium dioxide powder, *J. Am. Chem. Soc.*, 1977, **99**(1), 303–304.
56 K. Kalyanasundaram, Applications of functionalized transition metal complexes in photonic and optoelectronic devices, *Coord. Chem. Rev.*, 1998, **177**(1), 347–414.
57 G. Hodes, D. Cahen and J. Manassen, Tungsten trioxide as a photoanode for a photoelectrochemical cell (PEC), *Nature*, 1976, **260**(5549), 312–313.
58 J. H. Kennedy and K. W. Frese, Photooxidation of Water at α-Fe_2O_3 Electrodes, *J. Electrochem. Soc.*, 1978, **125**(5), 709–714.
59 A. B. Laursen, S. Kegnæs, S. Dahl and I. Chorkendorff, Molybdenum sulfides—efficient and viable materials for electro - and photoelectrocatalytic hydrogen evolution, *Energy Environ. Sci.*, 2012, **5**(2), 5577.
60 A. Guerrero and J. Bisquert, Perovskite semiconductors for photoelectrochemical water splitting applications, *Curr. Opin. Electrochem.*, 2017, **2**(1), 144–147.
61 A. S. Darsan and A. Pandikumar, Recent research progress on metal halide perovskite based visible light active photoanode for photoelectrochemical water splitting, *Mater. Sci. Semicond. Process.*, 2024, **174**, 108203.
62 W. Fan, Q. Lai, Q. Zhang and Y. Wang, Nanocomposites of TiO 2 and Reduced Graphene Oxide as Efficient Photocatalysts for Hydrogen Evolution, *J. Phys. Chem. C*, 2011, **115**(21), 10694–10701.
63 A. R. Marlinda, N. Yusoff, S. Sagadevan and M. R. Johan, Recent developments in reduced graphene oxide nanocomposites for photoelectrochemical water-splitting applications, *Int. J. Hydrogen Energy*, 2020, **45**(21), 11976–11994.
64 Y. P. Zhang, H. L. Tang, H. Dong, M. Y. Gao, C. C. Li and X. J. Sun, *et al.*, Covalent-organic framework based Z-scheme heterostructured noble-metal-free photocatalysts for visible-light-driven hydrogen evolution, *J. Mater. Chem. A*, 2020, **8**(8), 4334–4340.
65 B. Luan, X. Chu, Y. Wang, X. Qiao, Y. Jiang and F. Zhang, Construction of COF/COF Organic S-Scheme Heterostructure for Enhanced Overall Water Splitting, *Adv. Mater.*, 2024, **36**, 2412653.
66 J. Yu, X. Sun, X. Xu, C. Zhang and X. He, Donor-acceptor type triazine-based conjugated porous polymer for visible-light-driven photocatalytic hydrogen evolution, *Appl. Catal., B*, 2019, **257**, 117935.
67 Y. L. Wong, J. M. Tobin, Z. Xu and F. Vilela, Conjugated porous polymers for photocatalytic applications, *J. Mater. Chem. A*, 2016, **4**(48), 18677–18686.
68 G. B. Bodedla, M. Imran, J. Zhao, X. Zhu and W. Wong, Design of AIEgen-based porphyrin for efficient heterogeneous photocatalytic hydrogen evolution, *Aggregate*, 2023, **4**, e364.
69 G. B. Bodedla, V. Piradi, W. Thor, K. L. Wong, X. Zhu and W. Y. Wong, Self-assembly of Pt(II)-tetrakis(pentafluorophenyl)porphyrin *via* F···F interaction for efficient cocatalyst-free photocatalytic hydrogen evolution, *J. Mater. Chem. A*, 2024, **12**(5), 2924–2931.
70 G. B. Bodedla, V. Piradi, M. Imran, J. Zhao, X. Zhu and W. Y. Wong, Visible-to-near-infrared light-harvesting A–π–D–π–A porphyrins for boosted photocatalytic hydrogen evolution, *J. Mater. Chem. A*, 2023, **11**(3), 1473–1481.
71 S. Abednatanzi, P. Gohari Derakhshandeh, H. Depauw, F. X. Coudert, H. Vrielinck and P. Van Der Voort, *et al.*, Mixed-metal metal–organic frameworks, *Chem. Soc. Rev.*, 2019, **48**(9), 2535–2565.
72 L. Jiao, J. Y. R. Seow, W. S. Skinner, Z. U. Wang and H. L. Jiang, Metal–organic frameworks: Structures and functional applications, *Mater. Today*, 2019, **27**, 43–68.
73 S. L. James, Metal-organic frameworks, *Chem. Soc. Rev.*, 2003, **32**(5), 276.
74 A. Schneemann, V. Bon, I. Schwedler, I. Senkovska, S. Kaskel and R. A. Fischer, Flexible metal–organic frameworks, *Chem. Soc. Rev.*, 2014, **43**(16), 6062–6096.
75 D. Pugh, E. Ashworth, K. Robertson, L. C. Delmas, A. J. P. White and P. N. Horton, *et al.*, Metal–Organic Frameworks Constructed from Group 1 Metals (Li, Na) and Silicon-Centered Linkers, *Cryst. Growth Des.*, 2019, **19**(1), 487–497.
76 T. L. A. Nguyen, R. Demir-Cakan, T. Devic, M. Morcrette, T. Ahnfeldt and P. Auban-Senzier, *et al.*, 3-D Coordination Polymers Based on the Tetrathiafulvalenetetracarboxylate (TTF-TC) Derivative: Synthesis, Characterization, and Oxidation Issues, *Inorg. Chem.*, 2010, **49**(15), 7135–7143.
77 H. Deng, S. Grunder, K. E. Cordova, C. Valente, H. Furukawa and M. Hmadeh, *et al.*, Large-Pore Apertures in a Series of Metal-Organic Frameworks, *Science*, 2012, **336**(6084), 1018–1023.
78 J. Benecke, E. Svensson Grape, T. A. Engesser, A. K. Inge and H. Reinsch, Observation of three different linker

conformers in a scandium ferrocenedicarboxylate coordination polymer, *CrystEngComm*, 2020, **22**(34), 5569–5572.

79 D. Banerjee, S. J. Kim and J. B. Parise, Lithium Based Metal–Organic Framework with Exceptional Stability, *Cryst. Growth Des.*, 2009, **9**(5), 2500–2503.

80 Q. Z. Sun, Y. B. Yin, L. Y. Chai, H. Liu, P. F. Hao and X. P. Yan, *et al.*, A novel 3D heterometallic coordination complex with (3,4,5)-connected net topology: Synthesis, structure and luminescent property, *J. Mol. Struct.*, 2014, **1070**, 75–79.

81 F. M. Amombo Noa, M. Abrahamsson, E. Ahlberg, O. Cheung, C. R. Göb and C. J. McKenzie, *et al.*, A unified topology approach to dot-, rod-, and sheet-MOFs, *Chem*, 2021, **7**(9), 2491.

82 S. Smolders, T. Willhammar, A. Krajnc, K. Sentosun, M. T. Wharmby and K. A. Lomachenko, *et al.*, A Titanium(IV)-Based Metal–Organic Framework Featuring Defect-Rich Ti–O Sheets as an Oxidative Desulfurization Catalyst, *Angew. Chem., Int. Ed.*, 2019, **58**(27), 9160–9165.

83 Y. Peng, H. Huang, Y. Zhang, C. Kang, S. Chen and L. Song, *et al.*, A versatile MOF-based trap for heavy metal ion capture and dispersion, *Nat. Commun.*, 2018, **9**(1), 187.

84 Y. Kamakura, P. Chinapang, S. Masaoka, A. Saeki, K. Ogasawara and S. R. Nishitani, *et al.*, Semiconductive Nature of Lead-Based Metal–Organic Frameworks with Three-Dimensionally Extended Sulfur Secondary Building Units, *J. Am. Chem. Soc.*, 2020, **142**(1), 27–32.

85 D. W. Lee, V. Jo and K. M. Ok, $Sr_2[C_6H_3(CO_2)_3(NO_3)]\cdot$DMF: One-Dimensional Nano-Channel in a New Non-Centrosymmetric Strontium–Organic Framework with High Thermal Stability, *Cryst. Growth Des.*, 2011, **11**(7), 2698–2701.

86 Y. Fu, J. Su, Z. Zou, S. Yang, G. Li and F. Liao, *et al.*, Syntheses, Structures, and Gas Adsorption Properties of Two Novel Cadmium–Sodium Organic Frameworks with 1,3,5-Benzenetricarboxylate Ligands, *Cryst. Growth Des.*, 2011, **11**(8), 3529–3535.

87 D. Behera, P. Priyadarshini and K. Parida, ZIF-8 metal–organic frameworks and their hybrid materials: emerging photocatalysts for energy and environmental applications, *Dalton Trans.*, 2025, **54**, 2681–2708.

88 B. Chen, C. Liang, J. Yang, D. S. Contreras, Y. L. Clancy and E. B. Lobkovsky, *et al.*, A Microporous Metal–Organic Framework for Gas-Chromatographic Separation of Alkanes, *Angew. Chem., Int. Ed.*, 2006, **45**(9), 1390–1393.

89 J. Y. Lee, D. H. Olson, L. Pan, T. J. Emge and J. Li, Microporous Metal–Organic Frameworks with High Gas Sorption and Separation Capacity, *Adv. Funct. Mater.*, 2007, **17**(8), 1255.

90 A. Pichon, A. Lazuen-Garay and S. L. James, Solvent-free synthesis of a microporous metal–organic framework, *CrystEngComm*, 2006, **8**(3), 211.

91 G. Férey, C. Serre, C. Mellot-Draznieks, F. Millange, S. Surblé and J. Dutour, *et al.*, A Hybrid Solid with Giant Pores Prepared by a Combination of Targeted Chemistry, Simulation, and Powder Diffraction, *Angew. Chem., Int. Ed.*, 2004, **43**(46), 6296–6301.

92 B. Wang, A. P. Côté, H. Furukawa, M. O'Keeffe and O. M. Yaghi, Colossal cages in zeolitic imidazolate frameworks as selective carbon dioxide reservoirs, *Nature*, 2008, **453**(7192), 207–211.

93 H. Furukawa, N. Ko, Y. B. Go, N. Aratani, S. B. Choi and E. Choi, *et al.*, Ultrahigh Porosity in Metal-Organic Frameworks, *Science*, 2010, **329**(5990), 424–428.

94 S. T. Zheng, J. T. Bu, Y. Li, T. Wu, F. Zuo and P. Feng, *et al.*, Pore Space Partition and Charge Separation in Cage-within-Cage Indium–Organic Frameworks with High CO_2 Uptake, *J. Am. Chem. Soc.*, 2010, **132**(48), 17062–17064.

95 F. Zheng, D. Xiang, P. Li, Z. Zhang, C. Du and Z. Zhuang, *et al.*, Highly Conductive Bimetallic Ni–Fe Metal Organic Framework as a Novel Electrocatalyst for Water Oxidation. ACS Sustain, *Chem. Eng.*, 2019, **7**(11), 9743–9749.

96 L. Huang, G. Gao, H. Zhang, J. Chen, Y. Fang and S. Dong, Self-dissociation-assembly of ultrathin metal-organic framework nanosheet arrays for efficient oxygen evolution, *Nano Energy*, 2020, **68**, 104296.

97 A. Elaouni, M. El Ouardi, M. Zbair, A. BaQais, M. Saadi and H. Ait Ahsaine, ZIF-8 metal organic framework materials as a superb platform for the removal and photocatalytic degradation of organic pollutants: a review, *RSC Adv.*, 2022, **12**(49), 31801–31817.

98 S. Sadiq, I. Khan, M. Humayun, P. Wu, A. Khan and S. Khan, *et al.*, Synthesis of Metal–Organic Framework-Based ZIF-8@ZIF-67 Nanocomposites for Antibiotic Decomposition and Antibacterial Activities, *ACS Omega*, 2023, **8**(51), 49244–49258.

99 S. Demir, H. M. Çepni, N. Bilgin, M. Hołyńska and F. Yilmaz, Metal–organic frameworks based on copper(I) iodide and pyridine-3,5-dicarboxylic acid: Synthesis, crystal structures and luminescent properties, *Polyhedron*, 2016, **115**, 236–241.

100 H. Ji, K. Naveen, W. Lee, T. S. Kim, D. Kim and D. H. Cho, Pyridinium-Functionalized Ionic Metal–Organic Frameworks Designed as Bifunctional Catalysts for CO_2 Fixation into Cyclic Carbonates, *ACS Appl. Mater. Interfaces*, 2020, **12**(22), 24868–24876.

101 G. Luo, J. Jiang, S. Wei, C. Huang, D. Chen and B. Zhu, *et al.*, Introducing sulfonic acid polymers into MOF nanochannels for ultra-high Ba^{2+} adsorption capacity and proton conductivity, *Sep. Purif. Technol.*, 2024, **343**, 127133.

102 R. Ghorbani-Vaghei, D. A. Davood Azarifar, S. Daliran and A. R. Oveisi, The UiO-66-SO 3 H metal–organic framework as a green catalyst for the facile synthesis of dihydro-2-oxypyrrole derivatives, *RSC Adv.*, 2016, **6**(35), 29182–29189.

103 Y. Y. Enakieva, A. A. Sinelshchikova, M. S. Grigoriev, V. V. Chernyshev, K. A. Kovalenko and I. A. Stenina, *et al.*, Highly Proton-Conductive Zinc Metal-Organic Framework Based On Nickel(II) Porphyrinylphosphonate, *Chem. – Eur. J.*, 2019, **25**(45), 10552–10556.

104 K. Siemensmeyer, C. A. Peeples, P. Tholen, F. Schmitt, B. Çoşut and G. Hanna, *et al.*, Phosphonate Metal–Organic Frameworks: A Novel Family of Semiconductors, *Adv. Mater.*, 2020, **32**, 2000474.

105 A. Li, X. Yang and J. Chen, A novel route to size-controlled MIL-53(Fe) metal–organic frameworks for combined chemodynamic therapy and chemotherapy for cancer, *RSC Adv.*, 2021, **11**(18), 10540–10547.
106 F. Ahmadijokani, H. Molavi, M. Rezakazemi, S. Tajahmadi, A. Bahi and F. Ko, *et al.*, UiO-66 metal–organic frameworks in water treatment: A critical review, *Prog. Mater. Sci.*, 2022, **125**, 100904.
107 L. G. Gordeeva, M. V. Solovyeva and Y. I. Aristov, NH_2-MIL-125 as a promising material for adsorptive heat transformation and storage, *Energy*, 2016, **100**, 18–24.
108 D. J. Tranchemontagne, J. R. Hunt and O. M. Yaghi, Room temperature synthesis of metal-organic frameworks: MOF-5, MOF-74, MOF-177, MOF-199, and IRMOF-0, *Tetrahedron*, 2008, **64**(36), 8553–8557.
109 K. S. Lin, A. K. Adhikari, C. N. Ku, C. L. Chiang and H. Kuo, Synthesis and characterization of porous HKUST-1 metal organic frameworks for hydrogen storage, *Int. J. Hydrogen Energy*, 2012, **37**(18), 13865.
110 T. Panda, P. Pachfule, Y. Chen, J. Jiang and R. Banerjee, Amino functionalized zeolitic tetrazolate framework (ZTF) with high capacity for storage of carbon dioxide, *Chem. Commun.*, 2011, **47**(7), 2011–2013.
111 B. L. Bonnett, E. D. Smith, M. De La Garza, M. Cai, J. V. Haag and J. M. Serrano, *et al.*, PCN-222 Metal–Organic Framework Nanoparticles with Tunable Pore Size for Nanocomposite Reverse Osmosis Membranes, *ACS Appl. Mater. Interfaces*, 2020, **12**(13), 15765–15773.
112 S. Xie, Q. Qin, H. Liu, L. Jin, X. Wei and J. Liu, *et al.*, MOF-74-M (M = Mn, Co, Ni, Zn, MnCo, MnNi, and MnZn) for Low-Temperature NH 3 -SCR and In Situ DRIFTS Study Reaction Mechanism, *ACS Appl. Mater. Interfaces*, 2020, **12**(43), 48476–48485.
113 S. Yuan, L. Feng, K. Wang, J. Pang, M. Bosch and C. Lollar, *et al.*, Stable Metal–Organic Frameworks: Design, Synthesis, and Applications, *Adv. Mater.*, 2018, **30**, 1704303.
114 M. Eddaoudi, H. Li and O. M. Yaghi, Highly Porous and Stable Metal–Organic Frameworks: Structure Design and Sorption Properties, *J. Am. Chem. Soc.*, 2000, **122**(7), 1391–1397.
115 B. Li, H. Wang and B. Chen, Microporous Metal–Organic Frameworks for Gas Separation, *Chem. – Asian J.*, 2014, **9**(6), 1474–1498.
116 R. B. Lin, S. Xiang, H. Xing, W. Zhou and B. Chen, Exploration of porous metal–organic frameworks for gas separation and purification, *Coord. Chem. Rev.*, 2019, **378**, 87–103.
117 Z. Wang and S. M. Cohen, Postsynthetic modification of metal–organic frameworks, *Chem. Soc. Rev.*, 2009, **38**(5), 1315.
118 K. K. Tanabe and S. M. Cohen, Postsynthetic modification of metal–organic frameworks—a progress report, *Chem. Soc. Rev.*, 2011, **40**(2), 498–519.
119 N. L. Rosi, M. Eddaoudi, J. Kim, M. O'Keeffe and O. M. Yaghi, Advances in the chemistry of metal–organic frameworks, *CrystEngComm*, 2002, **4**(68), 401–404.
120 C. Wu and M. Zhao, Incorporation of Molecular Catalysts in Metal–Organic Frameworks for Highly Efficient Heterogeneous Catalysis, *Adv. Mater.*, 2017, **29**, 1605446.
121 O. M. Yaghi, M. O'Keeffe, N. W. Ockwig, H. K. Chae, M. Eddaoudi and J. Kim, Reticular synthesis and the design of new materials, *Nature*, 2003, **423**(6941), 705–714.
122 C. Wang, X. Liu, N. Keser Demir, J. P. Chen and K. Li, Applications of water stable metal–organic frameworks, *Chem. Soc. Rev.*, 2016, **45**(18), 5107–5134.
123 R. J. Kuppler, D. J. Timmons, Q. R. Fang, J. R. Li, T. A. Makal and M. D. Young, *et al.*, Potential applications of metal-organic frameworks, *Coord. Chem. Rev.*, 2009, **253**(23–24), 3042–3066.
124 D. Farrusseng, S. Aguado and C. Pinel, Metal–Organic Frameworks: Opportunities for Catalysis, *Angew. Chem., Int. Ed.*, 2009, **48**(41), 7502–7513.
125 Y. N. Gong, J. W. Liu, B. Z. Shao, D. C. Zhong and T. B. Lu, Stable metal–organic frameworks for PEC water splitting, *FlatChem*, 2021, **27**, 100240.
126 Y. An, Y. Liu, P. An, J. Dong, B. Xu and Y. Dai, *et al.*, Ni II Coordination to an Al-Based Metal–Organic Framework Made from 2-Aminoterephthalate for Photocatalytic Overall Water Splitting, *Angew. Chem., Int. Ed.*, 2017, **56**(11), 3036–3040.
127 Y. An, B. Xu, Y. Liu, Z. Wang, P. Wang and Y. Dai, *et al.*, Photocatalytic Overall Water Splitting over MIL-125(Ti) upon CoPi and Pt Co-catalyst Deposition, *ChemistryOpen*, 2017, **6**(6), 701–705.
128 S. Remiro-Buenamañana, M. Cabrero-Antonino, M. Martínez-Guanter, M. Álvaro, S. Navalón and H. García, Influence of co-catalysts on the photocatalytic activity of MIL-125(Ti)-NH2 in the overall water splitting, *Appl. Catal., B*, 2019, **254**, 677–684.
129 M. Cabrero-Antonino, J. Albero, C. García-Vallés, M. Álvaro, S. Navalón and H. García, Plasma-Induced Defects Enhance the Visible-Light Photocatalytic Activity of MIL-125(Ti)-NH2 for Overall Water Splitting, *Chem. – Eur. J.*, 2020, **26**(67), 15682–15689.
130 M. J. Beltrán-Leiva, D. Páez-Hernández and R. Arratia-Pérez, Theoretical Determination of Energy Transfer Processes and Influence of Symmetry in Lanthanide(III) Complexes: Methodological Considerations, *Inorg. Chem.*, 2018, **57**(9), 5120–5132.
131 Y. Wang, W. Xu, L. Lei, L. Chen, R. Ye and S. Xu, Photoluminescent NaGdF4@NaYF4:Ce/Tb inert-core/active-shell nanoparticles for selective and ultra-sensitive Cu^{2+} ions sensing, *J. Lumin.*, 2021, **235**, 118024.
132 Y. Kuang, J. Xu, C. Wang, T. Li, S. Gai and F. He, *et al.*, Fine-Tuning Ho-Based Red-Upconversion Luminescence by Altering $NaHoF_4$ Core Size and $NaYbF_4$ Shell Thickness, *Chem. Mater.*, 2019, **31**(19), 7898–7909.
133 S. Zhao, L. Li, X. Song, M. Zhu, Z. Hao and X. Meng, *et al.*, Lanthanide Ion Codoped Emitters for Tailoring Emission Trajectory and Temperature Sensing, *Adv. Funct. Mater.*, 2015, **25**(9), 1463–1469.
134 Y. Song, Y. Pi, X. Feng, K. Ni, Z. Xu and J. S. Chen, *et al.*, Cerium-Based Metal–Organic Layers Catalyze Hydrogen

Evolution Reaction through Dual Photoexcitation, *J. Am. Chem. Soc.*, 2020, **142**(15), 6866–6871.

135 C. V. Reddy, K. R. Reddy, V. A. Harish, J. Shim, M. V. Shankar, N. P. Shetti and T. M. Aminabhavi, *et al.*, Metal-organic frameworks (MOFs)-based efficient heterogeneous photocatalysts: Synthesis, properties and its applications in photocatalytic hydrogen generation, CO2 reduction and photodegradation of organic dyes, *Int. J. Hydrogen Energy*, 2020, **45**(13), 7656–7679.

136 S. Liu, C. Zhang, Y. Sun, Q. Chen, L. He and K. Zhang, *et al.*, Design of metal-organic framework-based photocatalysts for hydrogen generation, *Coord. Chem. Rev.*, 2020, **413**, 213266.

137 H. Luo, Z. Zeng, G. Zeng, C. Zhang, R. Xiao and D. Huang, *et al.*, Recent progress on metal-organic frameworks based-and derived-photocatalysts for water splitting, *Chem. Eng. J.*, 2020, **383**, 123196.

138 H. L. Nguyen, Metal–Organic Frameworks for Photocatalytic Water Splitting, *Solar RRL*, 2021, **5**, 2100198.

139 Y. Xiao, X. Guo, N. Yang and F. Zhang, Heterostructured MOFs photocatalysts for water splitting to produce hydrogen, *J. Energy Chem.*, 2021, **58**, 508–522.

140 X. Sun, K. Yuan and Y. Zhang, Advances and prospects of rare earth metal-organic frameworks in catalytic applications, *J. Rare Earths*, 2020, **38**(8), 801–818.

141 K. Sun, Y. Qian and H. Jiang, Metal-Organic Frameworks for Photocatalytic Water Splitting and CO_2 Reduction, *Angew. Chem.*, 2023, **135**, e202217565.

142 N. A. Nordin, M. A. Mohamed, M. N. I. Salehmin and S. F. Mohd Yusoff, Photocatalytic active metal–organic framework and its derivatives for solar-driven environmental remediation and renewable energy, *Coord. Chem. Rev.*, 2022, **468**, 214639.

143 F. Saraci, V. Quezada-Novoa, P. R. Donnarumma and A. J. Howarth, Rare-earth metal–organic frameworks: from structure to applications, *Chem. Soc. Rev.*, 2020, **49**(22), 7949–7977.

144 X. Shi, B. Cao, J. Liu, J. Zhang and Y. Du, Rare-Earth-Based Metal–Organic Frameworks as Multifunctional Platforms for Catalytic Conversion, *Small*, 2021, **17**, 2005371.

145 C. Fan, W. Dong, Y. Saira, Y. Tang, G. Fu and J. Lee, Rare-Earth–Modified Metal–Organic Frameworks and Derivatives for Photo/Electrocatalysis, *Small*, 2023, **19**, 2302738.

146 S. Meng, G. Li, P. Wang, M. He, X. Sun and Z. Li, Rare earth-based MOFs for photo/electrocatalysis, *Mater. Chem. Front.*, 2023, **7**(5), 806–827.

147 Y. Zhang, P. Wei, Z. Li, Y. Sun, Y. Liu and S. Huang, Advancements in rare earth metal-organic frameworks: Harnessing the power of photonics and beyond, *Coord. Chem. Rev.*, 2024, **514**, 215905.

148 Y. Zhang, S. Liu, Z. S. Zhao, Z. Wang, R. Zhang and L. Liu, *et al.*, Recent progress in lanthanide metal-organic frameworks and their derivatives in catalytic applications, *Inorg. Chem. Front.*, 2021, **8**, 590–619.

149 R. Rahimpour and A. Basile, Novel Catalysts Development for Hydrogen Production, *Int. J. Hydrogen Energy*, 2023, **48**(16), 6157.

150 A. Larimi, C. M. A. Parlett and Z. Jiang, Catalysis for sustainable hydrogen production, *Mater. Today Chem.*, 2023, **29**, 101457.

151 H. C. Zhou and S. Kitagawa, Metal–Organic Frameworks (MOFs), *Chem. Soc. Rev.*, 2014, **43**(16), 5415–5418.

152 J. W. Cheng, S. T. Zheng and G. Y. Yang, Diversity of crystal structure with different lanthanide ions involving in situ oxidation–hydrolysis reaction, *Dalton Trans.*, 2007, 4059.

153 B. Chen, Y. Yang, F. Zapata, G. Lin, G. Qian and E. B. Lobkovsky, Luminescent Open Metal Sites within a Metal–Organic Framework for Sensing Small Molecules, *Adv. Mater.*, 2007, **19**(13), 1693–1696.

154 A. R. Ramya, D. Sharma, S. Natarajan and M. L. P. Reddy, Highly Luminescent and Thermally Stable Lanthanide Coordination Polymers Designed from 4-(Dipyridin-2-yl)aminobenzoate: Efficient Energy Transfer from Tb^{3+} to Eu^{3+} in a Mixed Lanthanide Coordination Compound, *Inorg. Chem.*, 2012, **51**(16), 8818–8826.

155 T. Zhang and W. Lin, Metal–organic frameworks for artificial photosynthesis and photocatalysis, *Chem. Soc. Rev.*, 2014, **43**(16), 5982–5993.

156 N. H. Batubara and A. Zulys, Synthesis, Structural, Spectroscopic, and Morphology of Metal-Organic Frameworks Based on La (III) and Ligand 2,6-Napthalenedicarboxylic acid (La-MOFs) for Hydrogen Production, *IOP Conf. Ser.:-Mater. Sci. Eng.*, 2019, **546**(4), 042005.

157 A. Melillo, M. Cabrero-Antonino, S. Navalón, M. Álvaro, B. Ferrer and H. García, Enhancing visible-light photocatalytic activity for overall water splitting in UiO-66 by controlling metal node composition, *Appl. Catal., B*, 2020, **278**, 119345.

158 M. D. Allendorf, C. A. Bauer, R. K. Bhakta and R. J. T. Houk, Luminescent metal–organic frameworks, *Chem. Soc. Rev.*, 2009, **38**(5), 1330.

159 J. M. Zhou, W. Shi, N. Xu and P. Cheng, Highly Selective Luminescent Sensing of Fluoride and Organic Small-Molecule Pollutants Based on Novel Lanthanide Metal–Organic Frameworks, *Inorg. Chem.*, 2013, **52**(14), 8082–8090.

160 Q. Y. Yang, K. Li, J. Luo, M. Pan and C. Y. Su, A simple topological identification method for highly (3,12)-connected 3D MOFs showing anion exchange and luminescent properties, *Chem. Commun.*, 2011, **47**(14), 4234.

161 J. N. Hao and B. Yan, Ag^+-sensitized lanthanide luminescence in Ln 3+ post-functionalized metal–organic frameworks and Ag^+ sensing, *J. Mater. Chem. A*, 2015, **3**(9), 4788–4792.

162 D. Sun, W. Liu, M. Qiu, Y. Zhang and Z. Li, Introduction of a mediator for enhancing photocatalytic performance via post-synthetic metal exchange in metal–organic frameworks (MOFs), *Chem. Commun.*, 2015, **51**(11), 2056–2059.

163 A. Santiago Portillo, H. G. Baldoví, M. T. García Fernandez, S. Navalón, P. Atienzar and B. Ferrer, *et al.*, Ti as Mediator in the Photoinduced Electron Transfer of Mixed-Metal NH_2–UiO-66(Zr/Ti): Transient Absorption Spectroscopy Study and Application in Photovoltaic Cell, *J. Phys. Chem. C*, 2017, **121**(12), 7015–7024.

164 W. Liu, S. Zhang, B. Wu, X. Gong, J. Shao and S. Wang, *et al.*, Platinum-Assisted Bimetallic Ru–Eu/Pr MOFs for Photocatalytic H 2 Evolution from Water Splitting, *ACS Appl. Nano Mater.*, 2023, **6**(18), 16826–16836.

165 J. Gu, P. Zhao, W. Lin, J. Deng, Z. Chao and H. Jin, Cerium(III)-MOF as a photocatalyst for hydrogen evolution from water splitting, *Appl. Organomet. Chem.*, 2024, e7616.

166 P. Mahata, S. K. Mondal, D. K. Singha and P. Majee, Luminescent rare-earth-based MOFs as optical sensors, *Dalton Trans.*, 2017, **46**(2), 301–328.

167 F. Wang, Y. Pu, X. Zhang, F. Zhang, H. Cheng and Y. Zhao, A series of multifunctional lanthanide metal-organic frameworks for luminescent sensing and photocatalytic applications, *J. Lumin.*, 2019, **206**, 192–198.

168 Y. An, Y. Liu, H. Bian, Z. Wang, P. Wang and Z. Zheng, *et al.*, Improving the photocatalytic hydrogen evolution of UiO-67 by incorporating Ce^{4+}-coordinated bipyridinedicarboxylate ligands, *Sci. Bull.*, 2019, **64**(20), 1502.

169 H. Yang, L. Jia, Z. Zhang, B. Xu, Z. Liu and Q. Zhang, *et al.*, Novel cerium-based MOFs photocatalyst for photocarrier collaborative performance under visible light, *J. Catal.*, 2022, **405**, 74–83.

170 J. He, J. Wang, Y. Chen, J. Zhang, D. Duan and Y. Wang, *et al.*, A dye-sensitized Pt@UiO-66(Zr) metal–organic framework for visible-light photocatalytic hydrogen production, *Chem. Commun.*, 2014, **50**(53), 7063–7066.

171 C. Wang, Z. Xie, K. E. deKrafft and W. Lin, Doping Metal–Organic Frameworks for Water Oxidation, Carbon Dioxide Reduction, and Organic Photocatalysis, *J. Am. Chem. Soc.*, 2011, **133**(34), 13445–13454.

172 T. Toyao, M. Saito, S. Dohshi, K. Mochizuki, M. Iwata and H. Higashimura, *et al.*, Development of a Ru complex-incorporated MOF photocatalyst for hydrogen production under visible-light irradiation, *Chem. Commun.*, 2014, **50**(51), 6779.

173 C. C. Hou, T. T. Li, S. Cao, Y. Chen and W. F. Fu, Incorporation of a [Ru(dcbpy)(bpy) 2] 2+ photosensitizer and a Pt(dcbpy)Cl 2 catalyst into metal–organic frameworks for photocatalytic hydrogen evolution from aqueous solution, *J. Mater. Chem. A*, 2015, **3**(19), 10386–10394.

174 Y. Feng, C. Chen, Z. Liu, B. Fei, P. Lin and Q. Li, *et al.*, Application of a Ni mercaptopyrimidine MOF as highly efficient catalyst for sunlight-driven hydrogen generation, *J. Mater. Chem. A*, 2015, **3**(13), 7163–7169.

175 X. Sun, Q. Yu, F. Zhang, J. Wei and P. Yang, A dye-like ligand-based metal–organic framework for efficient photocatalytic hydrogen production from aqueous solution, *Catal. Sci. Technol.*, 2016, **6**(11), 3840–3844.

176 Q. Yu, H. Dong, X. Zhang, Y. X. Zhu, J. H. Wang and F. M. Zhang, *et al.*, Novel stable metal–organic framework photocatalyst for light-driven hydrogen production, *CrystEngComm*, 2018, **20**(23), 3228–3233.

177 S. Zhao, Q. Liang, W. Gao, M. Zhou, C. Yao and S. Xu, *et al.*, In Situ Growth of ZnIn 2 S 4 on MOF-Derived Ni–Fe LDH to Construct Ternary-Shelled Nanotubes for Efficient Photocatalytic Hydrogen Evolution, *Inorg. Chem.*, 2021, **60**(13), 9762–9772.

178 Z. Li, X. Wang, W. Tian, A. Meng and L. Yang, CoNi Bimetal Cocatalyst Modifying a Hierarchical $ZnIn_2S_4$ Nanosheet-Based Microsphere Noble-Metal-Free Photocatalyst for Efficient Visible-Light-Driven Photocatalytic Hydrogen Production. ACS Sustain, *Chem. Eng.*, 2019, **7**(24), 20190–20201.

179 J. Liu, G. Chen and J. Sun, Ag_2 S-Modified $ZnIn_2S_4$ Nanosheets for Photocatalytic H 2 Generation, *ACS Appl. Nano Mater.*, 2020, **3**(11), 11017–11024.

180 Q. Li, Y. Xia, C. Yang, K. Lv, M. Lei and M. Li, Building a direct Z-scheme heterojunction photocatalyst by $ZnIn_2S_4$ nanosheets and TiO_2 hollowspheres for highly-efficient artificial photosynthesis, *Chem. Eng. J.*, 2018, **349**, 287–296.

181 D. Kong, H. Fan, D. Yin, D. Zhang, X. Pu and S. Yao, *et al.*, $AgFeO_2$ Nanoparticle/$ZnIn_2S_4$ Microsphere p–n Heterojunctions with Hierarchical Nanostructures for Efficient Visible-Light-Driven H_2 Evolution. ACS Sustain, *Chem. Eng.*, 2021, **9**(7), 2673–2683.

182 Y. J. Yuan, D. Chen, J. Zhong, L. X. Yang, J. Wang and M. J. Liu, *et al.*, Interface engineering of a noble-metal-free 2D–2D MoS_2/Cu-$ZnIn_2S_4$ photocatalyst for enhanced photocatalytic H_2 production, *J. Mater. Chem. A*, 2017, **5**(30), 15771–15779.

183 J. Sowik, T. Grzyb, G. Trykowski, T. Klimczuk, K. Nikiforow and O. Cavdar, *et al.*, Lanthanide-organic-frameworks modified $ZnIn_2S_4$ for boosting hydrogen generation under UV-Vis and visible light, *Int. J. Hydrogen Energy*, 2022, **47**(36), 16065–16079.

184 T. T. Li, Y. Chen, Y. Cheng, M. Q. Zheng, J. F. Qian and M. Y. He, *et al.*, Synthesis of rare earth MOF/CZS materials derived from aromatic tetracarboxylic acids and photocatalytic hydrogen production, *Int. J. Hydrogen Energy*, 2024, **65**, 225–235.

185 J. Kundu, D. D. Mal and D. Pradhan, Single-step solvothermal synthesis of highly uniform $Cd_xZn_{1-x}S$ nanospheres for improved visible light photocatalytic hydrogen generation, *Inorg. Chem. Front.*, 2021, **8**(12), 3055–3065.

186 L. Zhang, Z. Jin, S. Huang, Y. Zhang, M. Zhang and Y. J. Zeng, *et al.*, Ce-Doped Graphitic Carbon Nitride Derived from Metal Organic Frameworks as a Visible Light-Responsive Photocatalyst for H2 Production, *Nanomaterials*, 2019, **9**(11), 1539.

187 J. Hao, W. Zhan, L. Sun, G. Zhuang, X. Wang and X. Han, Combining N,S-Codoped C and CeO_2: A Unique Hinge-like Structure for Efficient Photocatalytic Hydrogen Evolution, *Inorg. Chem.*, 2020, **59**(1), 937–942.

188 P. Wu, X. Guo, L. Cheng, C. He, J. Wang and C. Duan, Photoactive Metal-Organic Framework and Its Film for Light-Driven Hydrogen Production and Carbon Dioxide Reduction, *Inorg. Chem.*, 2016, **55**(16), 8153–8159.

189 S. L. Anderson, D. Tiana, C. P. Ireland, G. Capano, M. Fumanal and A. Gładysiak, *et al.*, Taking lanthanides out of isolation: tuning the optical properties of metal–organic frameworks, *Chem. Sci.*, 2020, **11**(16), 4164–4170.

190 Y. Hidalgo-Rosa, M. Saavedra-Torres, B. D. Koivisto, M. A. Treto-Suárez, D. Páez-Hernández and X. Zarate,

et al., Rare-earth-based metal–organic frameworks with improved visible-light-harvesting properties: a quantum chemistry study, *J. Mater. Sci.*, 2023, **58**(21), 8862–8877.

191 P. Mahata, K. V. Ramya and S. Natarajan, Pillaring of $CdCl_2$-Like Layers in Lanthanide Metal–Organic Frameworks: Synthesis, Structure, and Photophysical Properties, *Chem. – Eur. J.*, 2008, **14**(19), 5839–5850.

192 P. Mahata, K. V. Ramya and S. Natarajan, Synthesis, structure and optical properties of rare-earth benzene carboxylates, *Dalton Trans.*, 2007, 4017.

193 J. Yang, Q. Yue, G. D. Li, J. J. Cao, G. H. Li and J. S. Chen, Structures, Photoluminescence, Up-Conversion, and Magnetism of 2D and 3D Rare-Earth Coordination Polymers with Multicarboxylate Linkages, *Inorg. Chem.*, 2006, **45**(7), 2857–2865.